Supplementary Information (SI) for Journal of Materials Chemistry A.

Supporting Information

Lattice strain induced electronic effects on heteroatom-doped nickel alloy catalyst for electrochemical water splitting

Shouvik Mete,[a] Manish S. Sengar,[b] Marshal Dhayal,[b] Vijay Kumar,[c, d] and Santosh K. Singh*,[a]

[a]Electrochemical Energy Laboratory, Department of Chemistry, School of Natural Sciences, Shiv Nadar Institution of Eminence, Dadri, Uttar Pradesh-201314, India

[b]Plasma Processing and Biophysics Laboratory, Department of Physics, IIT Delhi-110016, India

[c]Center for Informatics, School of Natural Sciences, Shiv Nadar Institution of Eminence, Dadri, Uttar Pradesh-201314, India

[d]Dr. Vijay Kumar Foundation, 1969 Sector 4, Gurgaon, Haryana -122001, India

*Email: santoshk.singh@snu.edu.in

1. Experimental Section

1.1. Materials: Potassium hydroxide (KOH), manganese(II) nitrate hydrate (98%, MnN_2O_6. xH_2O), iron(II) chloride tetrahydrate (98%, $Cl_2Fe.4H_2O$), iron(III) nitrate nonahydrate (≥98%, $Fe(NO_3)_3.9H_2O$), cobalt(II) nitrate hexahydrate (≥98%, $Co(NO_3)_2 \cdot 6H_2O$), copper(II) nitrate trihydrate (≥99%, $Cu(NO_3)_2 \cdot 3H_2O$), 20% Pt/C and ruthenium(IV) oxide (RuO_2) was procured from Sigma Aldrich and used without further purification. Nickel foam (foam size-66x300 mm, thickness-1.6 mm, PPI-95) was purchased from Nano Research Elements and used after sonication and washing under water followed by acetone.

1.2. Characterization techniques: X-ray diffraction analysis was carried out using a PANalytical instrument using Cu Kα radiation (λ = 1.54 Å) at the scan rate of 5°/min. X-ray photoelectron spectroscopy (XPS) analyses were carried out with a spectrophotometer ESCALAB-250Xi model equipped with Al-Kα monochromatic X-ray source (20 mA, 15 kV) operated under ultra-high vacuum (7×10^{-9} bar) at room temperature with the spot size of 650 μm. The reference C1s signal at 284.8 eV was used to correct all the reported binding energies. XPS data were analyzed by using CASA XPS software. For the scanning electron microscopy (SEM) and energy dispersive X-ray (EDX) analysis, the JEOL JSM-7610 Plus model instrument with a detector of an electron acceleration voltage of 15 kV was used to examine the surface morphology and elemental ratio of the samples. The transmission electron microscopy (TEM) was performed by using a JEOL HJEM-ARM200F NEOARM instrument. The electrochemical analysis was carried out using an SP-300/240 model Biologic potentiostat. The X-ray fluorescence (XRF) spectroscopy of the surface for the elemental analysis was carried out using Shimadzu EDX-7200 instrument.

1.3. Preparation of M-doped Ni electrode: For the fabrication of heteroatom doped free-standing electrode, the dopant (Mn, Fe, Co, and Cu) metal salt's solution of 2M concentration was prepared. Subsequently, the washed nickel (Ni) foam of geometric area of $1.0*0.25\ cm^2$ was dipped in 2 ml solutions for 10 min to establish the galvanic exchange followed by deposition over the surface of pristine Ni foam (i.e., ion-exchange between the Ni-foam and dopant metal). The obtained ion-exchanged Ni-foam foam was further heat treated at 200 ℃ for 2 hrs. in a muffle furnace with a temperature ramping 10 ℃/min in atmosphere pressure to get the alloy phase. The heat-treated electrodes were washed thoroughly with water using bath sonication to remove the unreacted metal ions. Then, the electrodes were dried at 60 ℃ for 8 hrs. and stored for further use.

The resulting M-Ni (M=Mn, Fe, Co, and Cu) alloy fee standing electrode with an accessible geometric surface area of 0.5 (l)*0.25 (w) cm^2 held by an electrode holder was directly employed as a working electrode. All the electro-catalytic HER/OER half-cell reactions were carried out in the same procedure.

1.4 Preparation of the-state-of-the-art Pt/C and RuO_2 electrode

For the coating of material over the glassy carbon electrode, catalyst slurry was prepared by dispersing 5 mg of the 20% Pt/C and RuO_2 catalyst powder in 1 ml IPA: water mixture (3:2) with the addition of 40 μL Nafion® solution (5 %). The resulting mixture was ultrasonicated for 5 min followed by bath sonication for 30 min to get the homogeneous dispersed solution. Before coating the catalysts over the glassy carbon electrode, a 3 mm (inner radius) glassy carbon electrode (GCE) surface was polished with 0.05 and 1.0 μm alumina slurries, and a polishing pad was washed properly with water and ethanol to avoid contamination. To the polished GCE, 10 μL of the Pt/C catalyst slurry or 15 μL of the prepared slurry was coated and dried under an IR lamp. The dried electrode was used as a working electrode for electrochemical analysis.

1.5. Electrochemical measurement

All the electrochemical studies were performed using a Biologic instruments potentiostat in a conventional three-electrode test cell. Measurements were performed under N_2 saturated 0.1 M KOH electrolyte (pH=13.2). For the studies of OER and HER reactions, a platinum wire, and a Hg/HgO electrode were used as counter and reference electrodes. The geometrical surface area for the geometrical current density of conversion is 0.25 cm^2. The recorded potentials have been converted to the reversible hydrogen electrode (RHE) using the below equation.[1]

$$E_{RHE} = E_{Hg/HgO} + 0.0591pH + E^0_{Hg/HgO} \qquad (1)$$

The CV and LSV for the OER/HER measurements for the 20% Pt/C and RuO_2 were carried out using a glassy carbon (GC) working electrode with an area of 0.07065 cm^2. The CV and LSV experiments were carried out at a scan rate of 10 and 5 mV s^-

[1]. The rotation of electrodes was set at 900 and 1600 rpm for CV and LSV respectively.

1.6. Electrochemically active surface area (ECSA) calculation

The electrochemical active surface area (ECSA) is proportional to the electrochemical double layer capacitance (C_{dl}), and the ECSA value can be calculated using the following equation.

$$\mathrm{ECSA} = C_{dl}/C_s \qquad (2)$$

Where C_s is the specific capacitance of a flat working electrode. The double-layer capacitance (C_{dl}) is calculated from the slope of j (mA cm^{-2}) with anodic peak current (Ja) and cathodic peak current (Jc) vs. scan rate plot from **Figure S13, 19-21.**

1.7. Open circuit voltage measurement

To monitor the galvanic ion exchange between Ni and heteroatom ion (Mn^{2+}, Fe^{2+}, Co^{2+}, and Cu^{2+}), an open circuit voltage (OCV) measurement was carried out. In a three-electrode electrochemical cell, the pristine Ni foam electrode was dipped in 5 ml of de-ionized H_2O (18.2 MΩ cm) along with Pt wire and Ag/AgCl electrode. The bare electron transfer of Ni foam was recorded up to ~4 min. The heteroatom ion solution of 500µl was quickly injected into the system. The oxidation and reduction reactions were monitored as a function of change in outcome voltage.

1.8. Determination of turnover frequency (TOF)

The TOF value for OER and HER experiments can be calculated as described in the equation reported previously.[2]

$$\mathrm{TOF} = \frac{j\,N_A}{F\eta\Gamma} \qquad (3)$$

Where, j = current density (mA cm^{-2}), N_A = Avogadro constant (6.0221×10^{23} mol^{-1}), n is the number of electrons transferred = 4 for OER, F = Faraday constant (96485 A mol^{-1}) and Γ is the surface or total concentration of catalyst in terms of the number of atoms.

Surface area of nickel foam = (0.25*0.5) cm^2 = 0.125 cm^2

As both sides of Ni foam participate in the reaction, the actual surface area is 0.25 cm^2.

The calculated area associated with the oxidation of Ni^{2+} to Ni^{3+} of Ni, NiMn, NiFe, NiCo, and NiCu synthesized catalyst, as depicted in **Figure S14.**

For pristine Ni, the associated charge = (1.821×10^{-5} V A)/ 0.01 V s^{-1}

= 1.821×10^{-3} A s =1.821×10^{-3} C.

So, the number of electron transferred = $1.821 \times 10^{-3} / 1.602 \times 10^{-19} = 11.3 \times 10^{15}$

Since the oxidation of Ni^{2+} to Ni^{3+} is a single electron transfer reaction, the number of electrons calculated above is exactly the same as the number of surface-active sites

Similarly, the number of electrons transferred for NiMn, NiFe, NiCo, and NiCu are 11.21×10^{15}, 11.8×10^{15}, $27.7\times 10^{15,}$ and 46.2×10^{15} respectively.

TOF value of pristine Ni at 1.66 V vs. RHE for OER,

$$\boldsymbol{TOF} = \frac{j\,N_A}{F\eta\Gamma} = \frac{24\ \times\ 10^{-3}\ A\,cm^{-2} \times \left(6.0221\ \times 10^{23} atoms\ mole^{-1}\right)}{96485\ A\,mol^{-1} \times 4 \times \left(11.21 \times 10^{15} atom\ cm^{-2}\right)}$$

$\boldsymbol{TOF}_{\mathbf{1.66}\ \boldsymbol{V}}$ = 3.31 s^{-1}

Similarly, the calculated TOF at 1.66 V condition for NiMn, NiFe, NiCo, and NiCu are 10.44, 23.53, 2.09, and 1.4 s^{-1} respectively.

We can calculate the TOF for HER reaction as well by using the same surface concentration of the Ni site. To calculate the TOF, we have to take n =2 along with the geometrical current density in a specific voltage.

$$\boldsymbol{TOF} = \frac{j\,N_A}{F\eta\Gamma} = \frac{7.28\ \times\ 10^{-3}\ A\,cm^{-2} \times \left(6.0221\ \times 10^{23} atoms\ mole^{-1}\right)}{96485\ A\,mol^{-1} \times 2 \times \left(11.21 \times 10^{15} atom\ cm^{-2}\right)}$$

$\boldsymbol{TOF}_{\mathbf{-0.3\,V}}$ = 2.01 s^{-1}

Here, we have calculated TOF at -0.3 V condition for NiMn, NiFe, NiCo, and NiCu are 2.01, 5.74, 6.23, 2.60, and 1.91 s^{-1} respectively.

1.9. Theoretical calculations

The density functional theory (DFT) calculations were carried out on a 5-layer slab using Vienna ab initio simulation program (VASP).[3] For the exchange-correlation functional we used generalized gradient approximation (GGA) of Perdew-Burke-Ernzerhof (PBE)[4] and the electron ion interaction has been treated using projected-augmented wave (PAW) pseudopotential method.[5] The tolerance for the total energy convergence was 10^{-5} eV and cut-off energy for the plane wave basis sets was set at 400 eV. The tolerance for the force on each ion was taken to be 0.005 eV/A. A 4x4x1 supercell of 5-layered Ni (111) was built with a vacuum space of about 15 Å. Upper three layers were doped with 10% dopant atoms for these separate calculations were done by taking 2x2x2 supercell with about 10% dopant and the structure was optimized and resulting lattice parameters was used and kept fixed in the XY plane. While along the Z-direction the ions were fully relaxed. The bottom two layers of the Ni slab was fixed considering as bulk layers. A (3 x 3 x 1) k-point grid was used for the Brillouin zone integrations for the supercell of the slab. The lattice parameters in the plane of the layers were kept fixed with the bulk values and ions were relaxed until the absolute value of each component of the force became less than 0.005 eV/Å. All the calculations were done with spin polarization.

2.0 Experimental Results

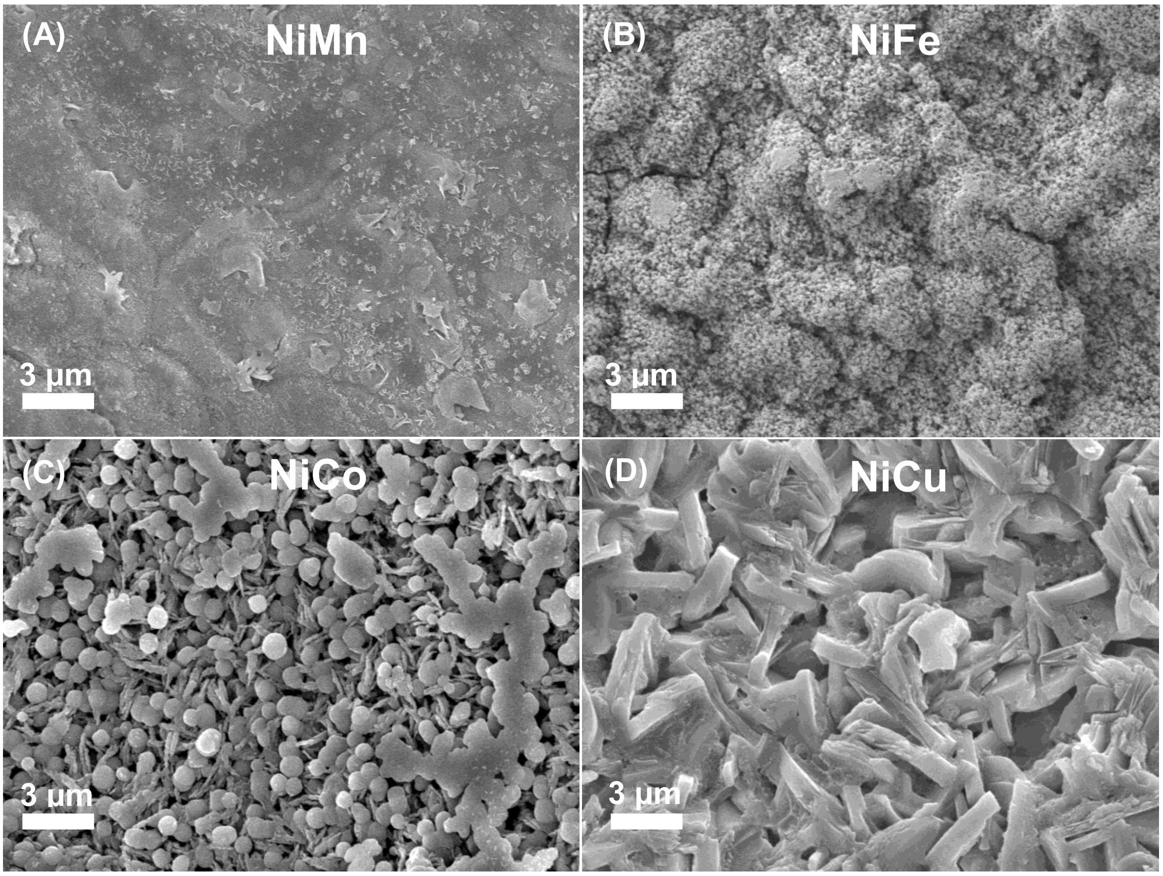

Figure S1. Field emission scanning electron microscopy (FESEM) images of synthesized electrode surfaces using 3M dopant metal ion concentration, (A) NiMn, (NiFe), (C) NiCo, and (D) NiCu.

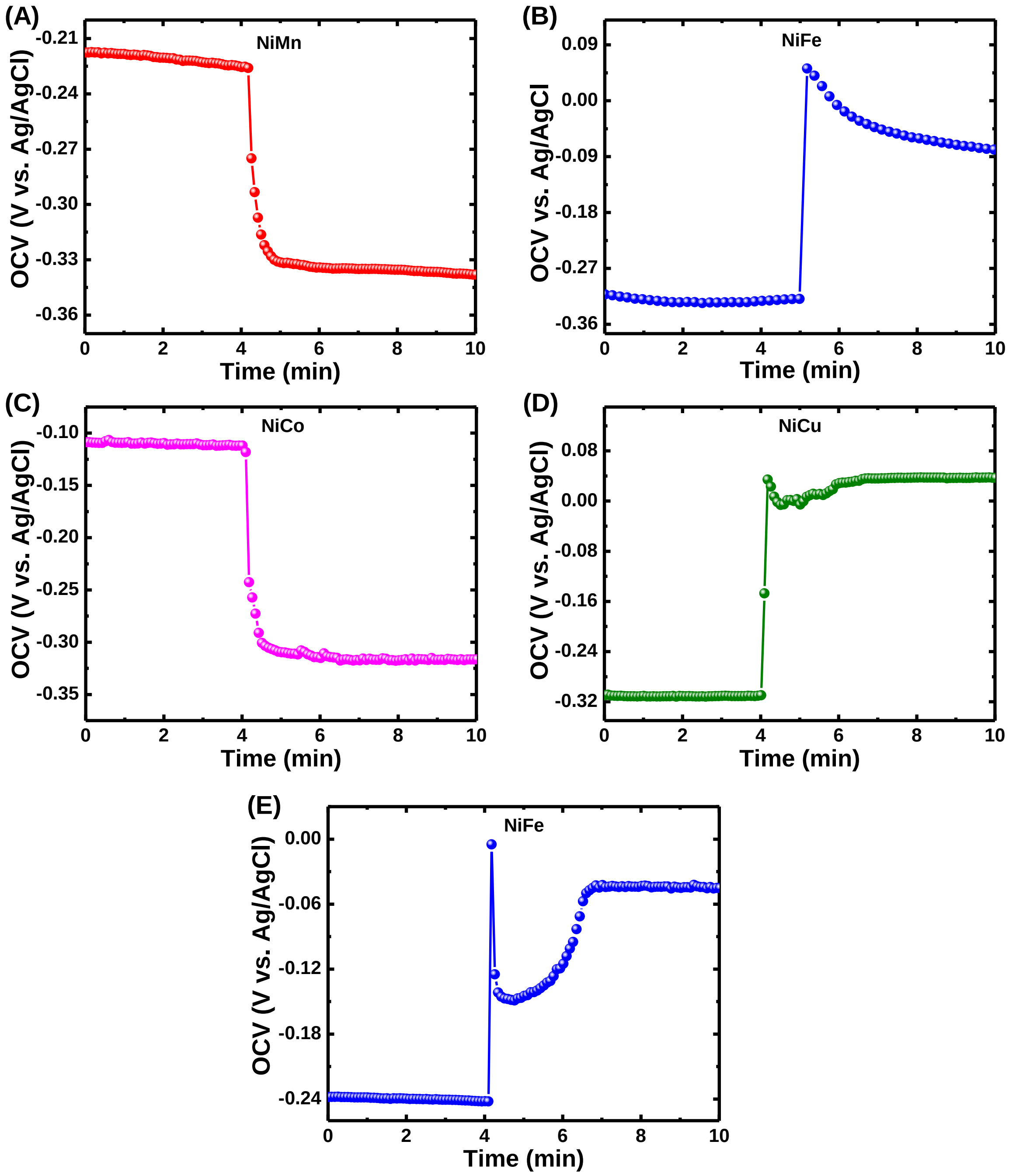

Figure S2. Open circuit voltage (OCV) measurement during the ion exchange process between Ni foam and heteroatom ion (Mn^{2+}, Fe^{2+}, Co^{2+}, and Cu^{2+}). Initial voltage shifts downwards and upward support the reduction and oxidation of Ni, respectively. OCV data of (A) Mn^{2+} ions exchange, (B) Fe^{2+} ions exchange, (C) Co^{2+} ions exchange, (D) Cu^{2+} ions exchange, and (E) Fe^{3+} ions exchange.

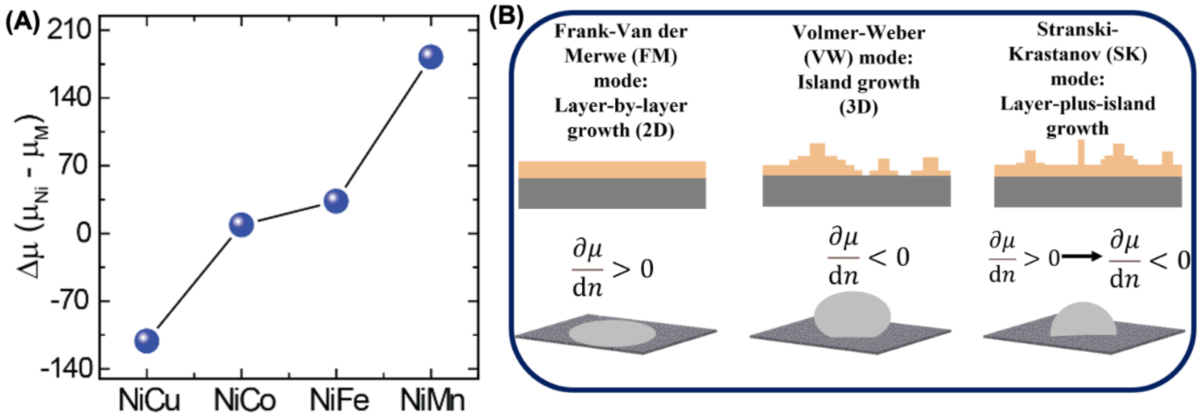

Figure S3: Surface particle growth mechanism with a chemical potential difference of synthesized electrodes; (A) chemical potential (∆μ) between the Ni substrate and dopant metal atoms, and (B) different epitaxial growth mechanism variation with the correlation of μ.[6]

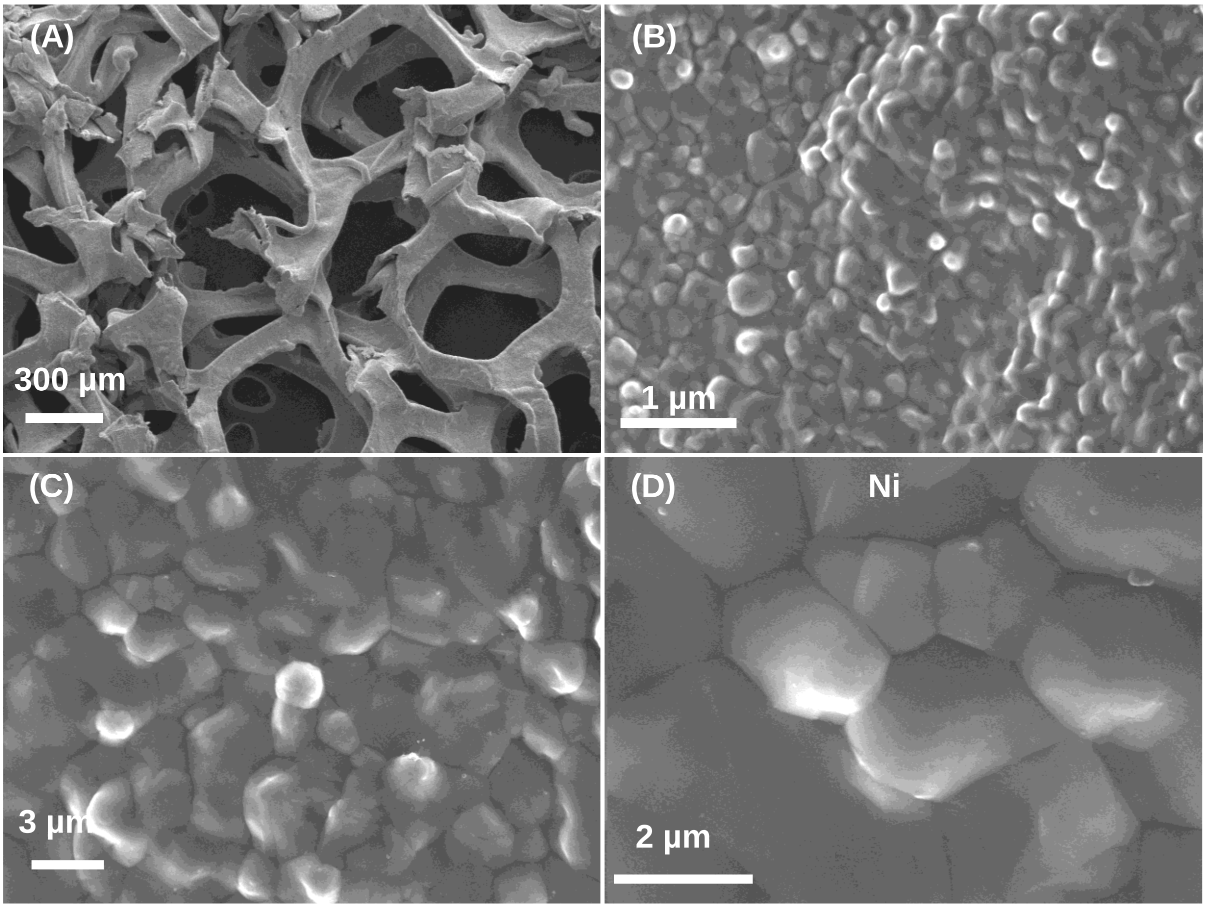

Figure S4. Field emission scanning electron microscopy (FESEM) analysis of the pristine Ni at various magnifications of (A) ×43 (B) ×2000, (C) ×5000, and (D) ×15000.

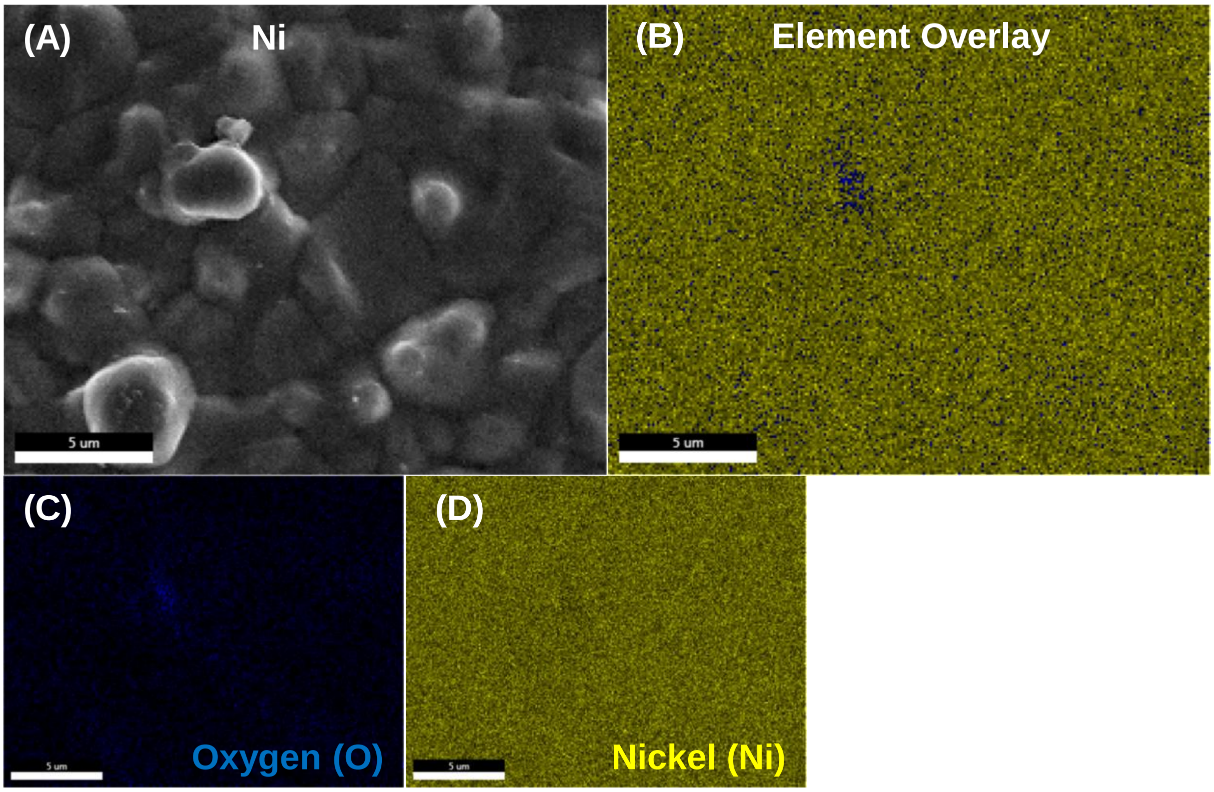

Figure S5. FESEM mapping image of Ni electrode and elemental mapping; (A) Ni electrode surface morphology, (B-D) surface elemental mapping of the Ni electrode surface showing the distribution of O and Ni.

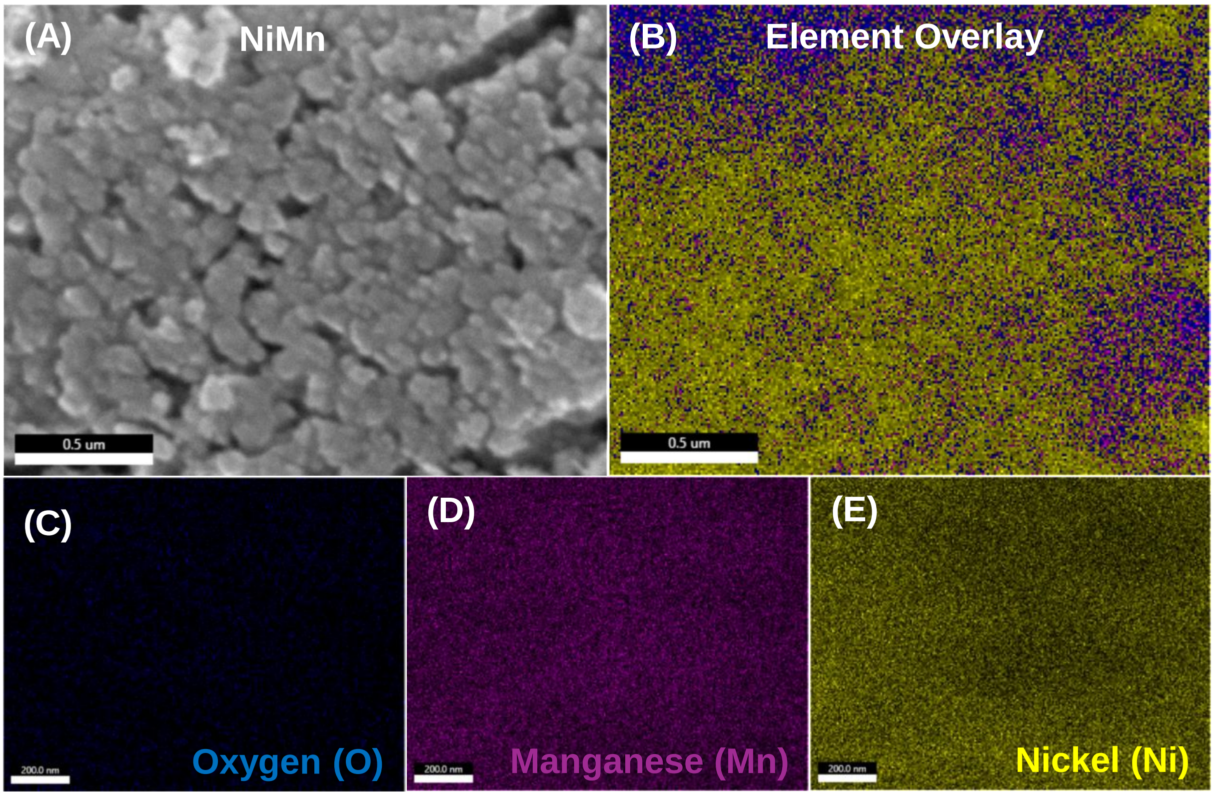

Figure S6. FESEM image and elemental mapping of NiMn-alloy electrode; (A) Area of NiMn electrode surface used for the elemental mapping; (B-E) the distribution of O, Mn, and Ni over the NiMn electrode surface.

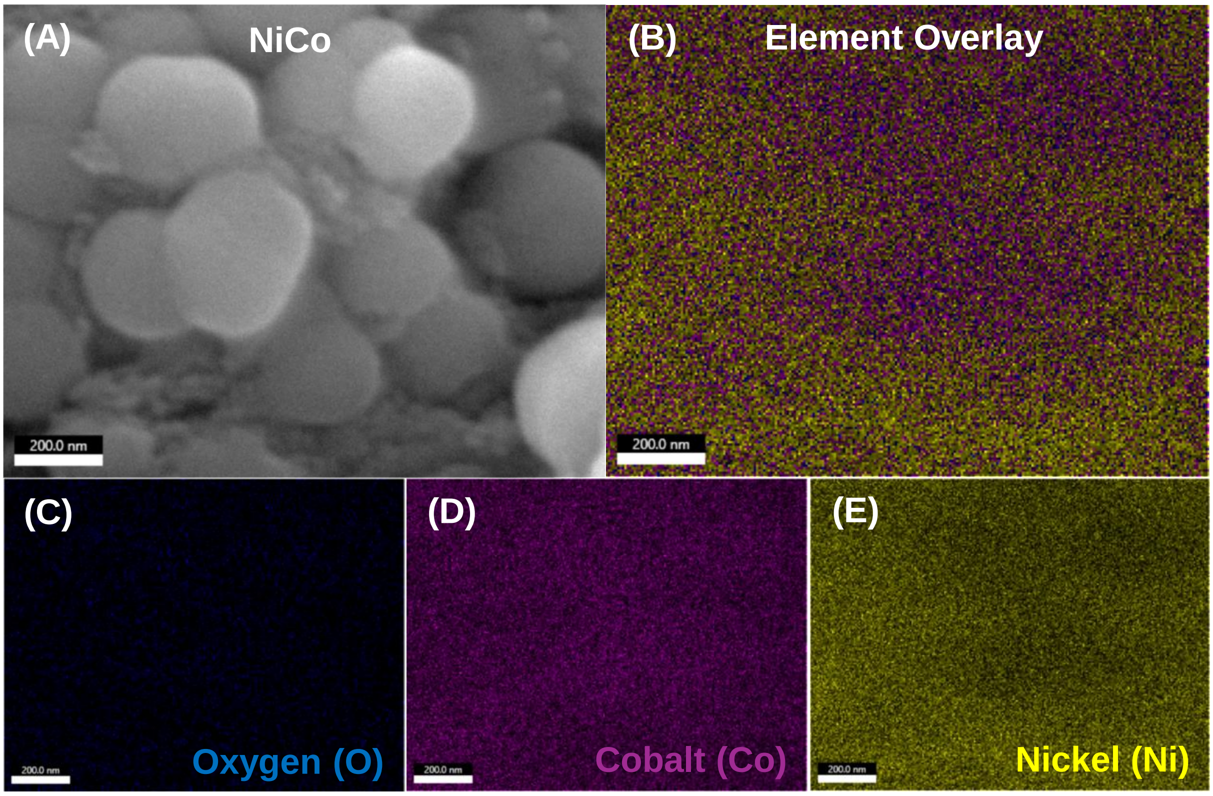

Figure S7. FESEM image and elemental mapping of NiCo electrode; (A) area of NiCo electrode surface used for the elemental mapping; (B-E) the distribution of O, Co, and Ni over the electrode surface.

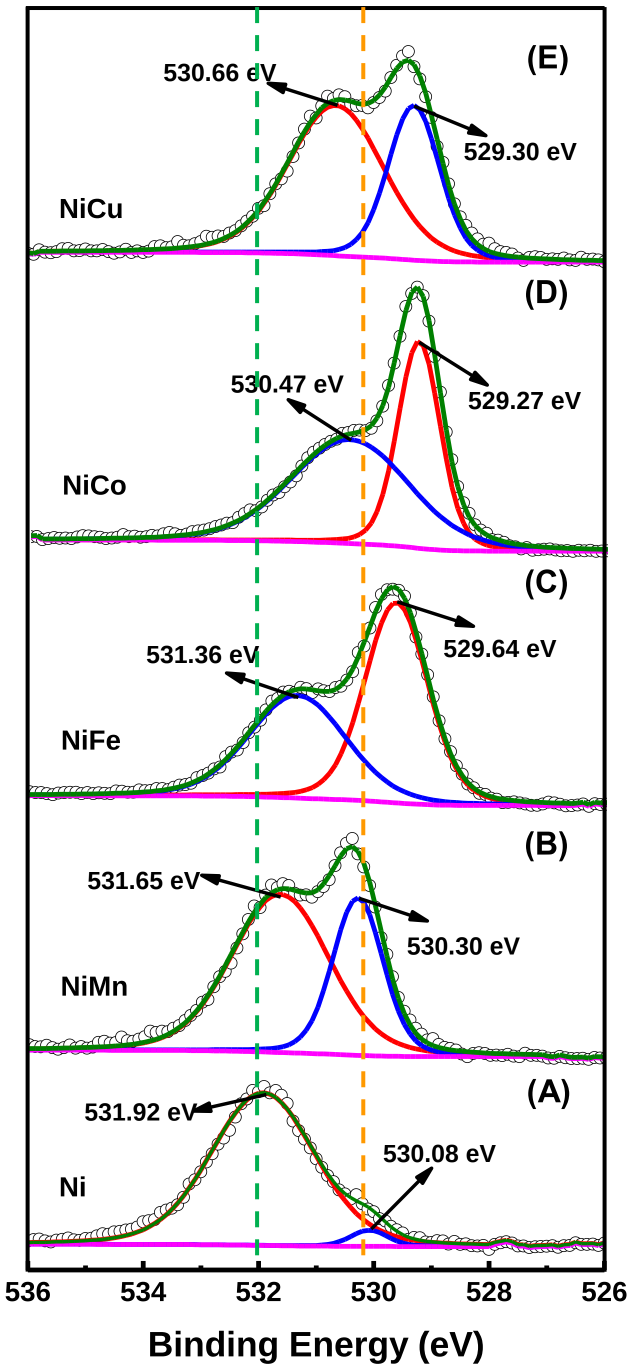

Figure S8. Deconvoluted XPS O1s spectra of (A) Ni, (B) NiMn, (C) NiFe, (D) NiCo, and (E) NiCu electrode.

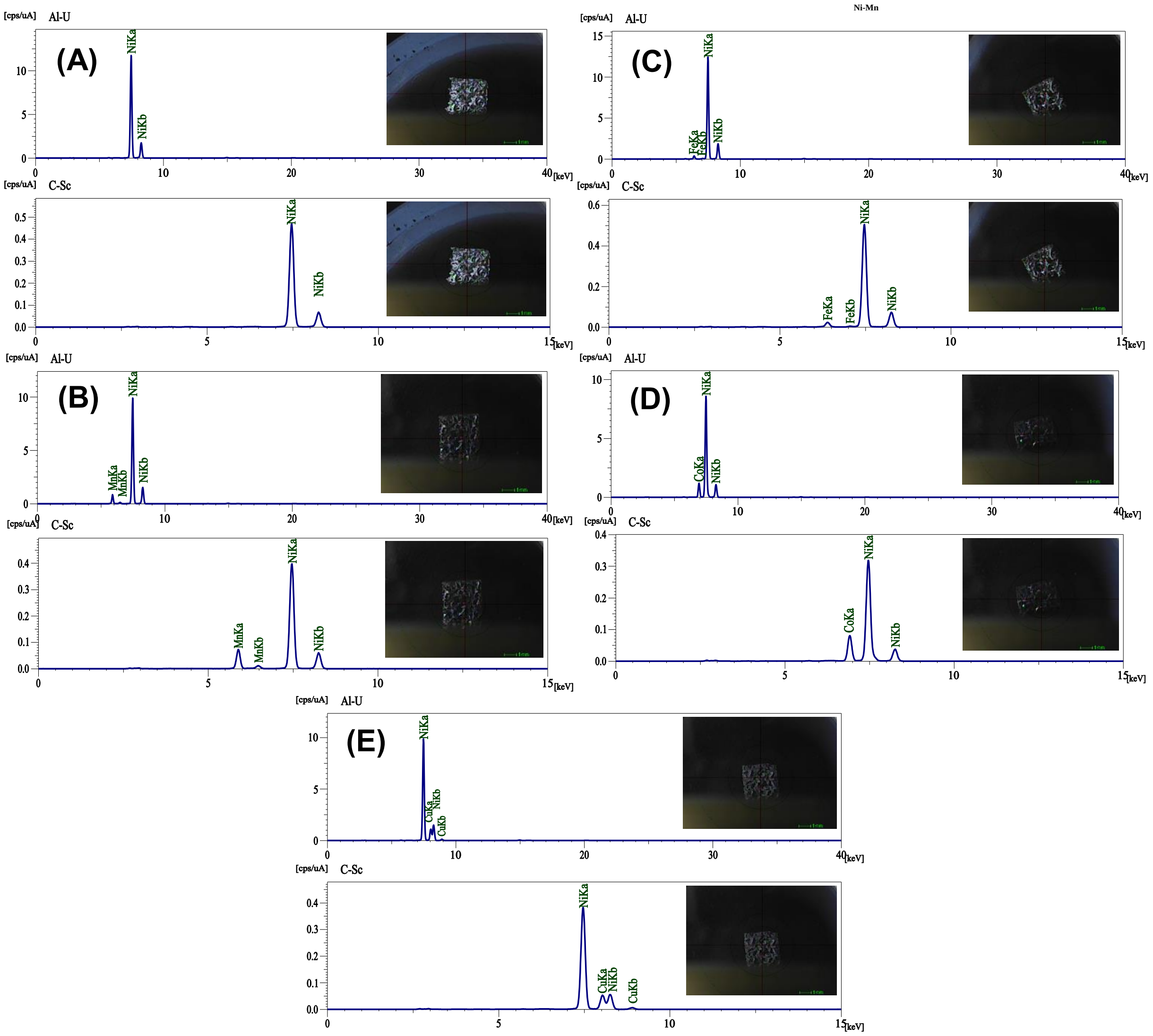

Figure S9. X-ray fluorescence (XRF) analysis of Ni-M (M = Mn, Fe, Co, Cu) alloy electrodes to determine elemental composition (A) Ni, (B) NiMn, (C) NiFe, (D) NiCo, and (E) NiCu electrode.

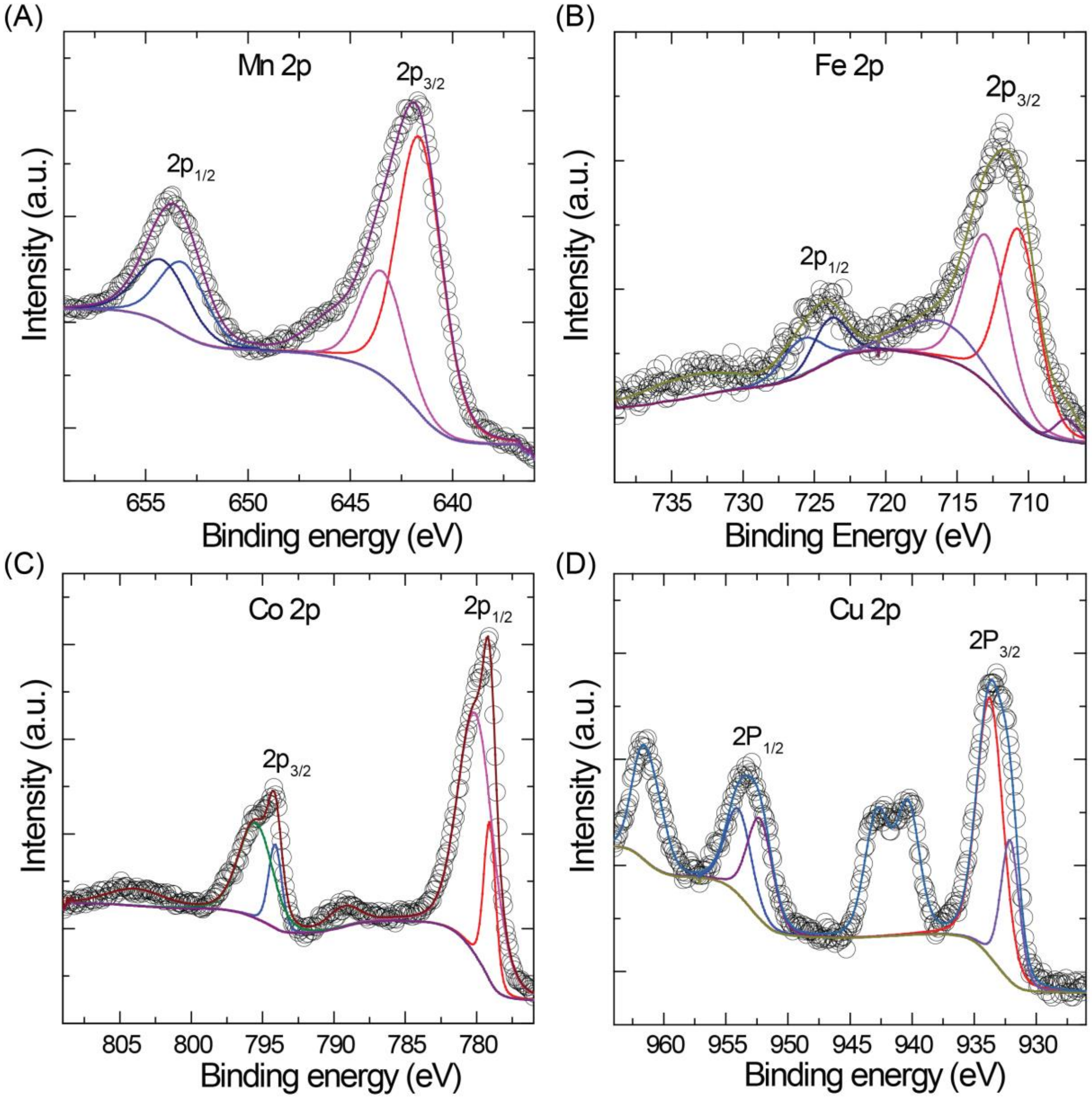

Figure S10. Deconvoluted high-resolution X-ray photoelectron spectroscopy (XPS) analysis of the dopant elements presents in Ni-M alloy electrode (A) Mn 2p, (B) Fe 2p, (C) Co 2p, and (D) Cu 2p.

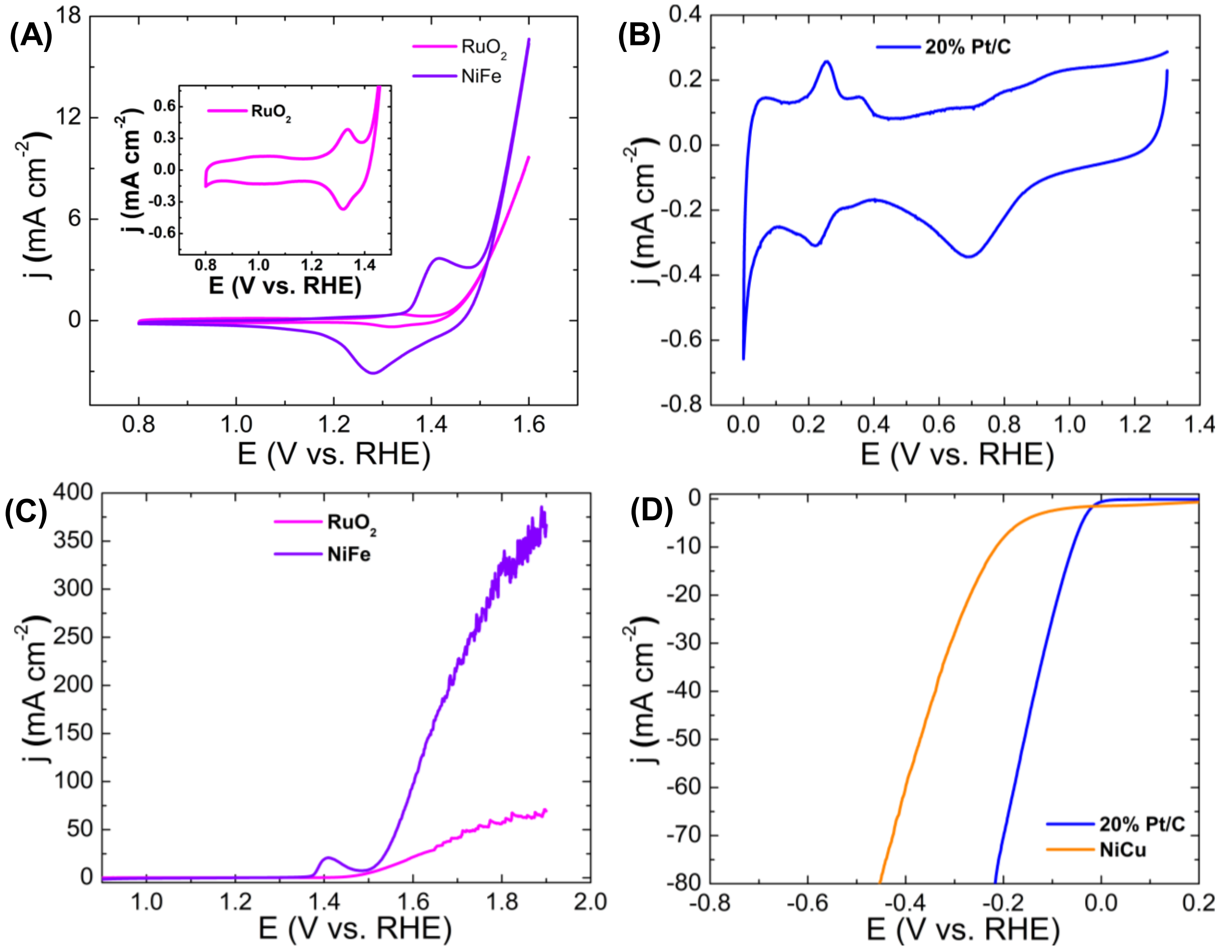

Figure S11. Comparative cyclic voltammogram (CV) and linear sweep voltammogram (LSV) analysis of state-of-the-art electrocatalyst in 0.1M KOH electrolyte; (A) comparative CV of RuO_2 and NiFe; (B) CV of 20% Pt/C; (C) comparative OER LSV polarization study between RuO_2 and NiFe; (D) comparative HER LSV polarization study between 20% Pt/C and NiCu.

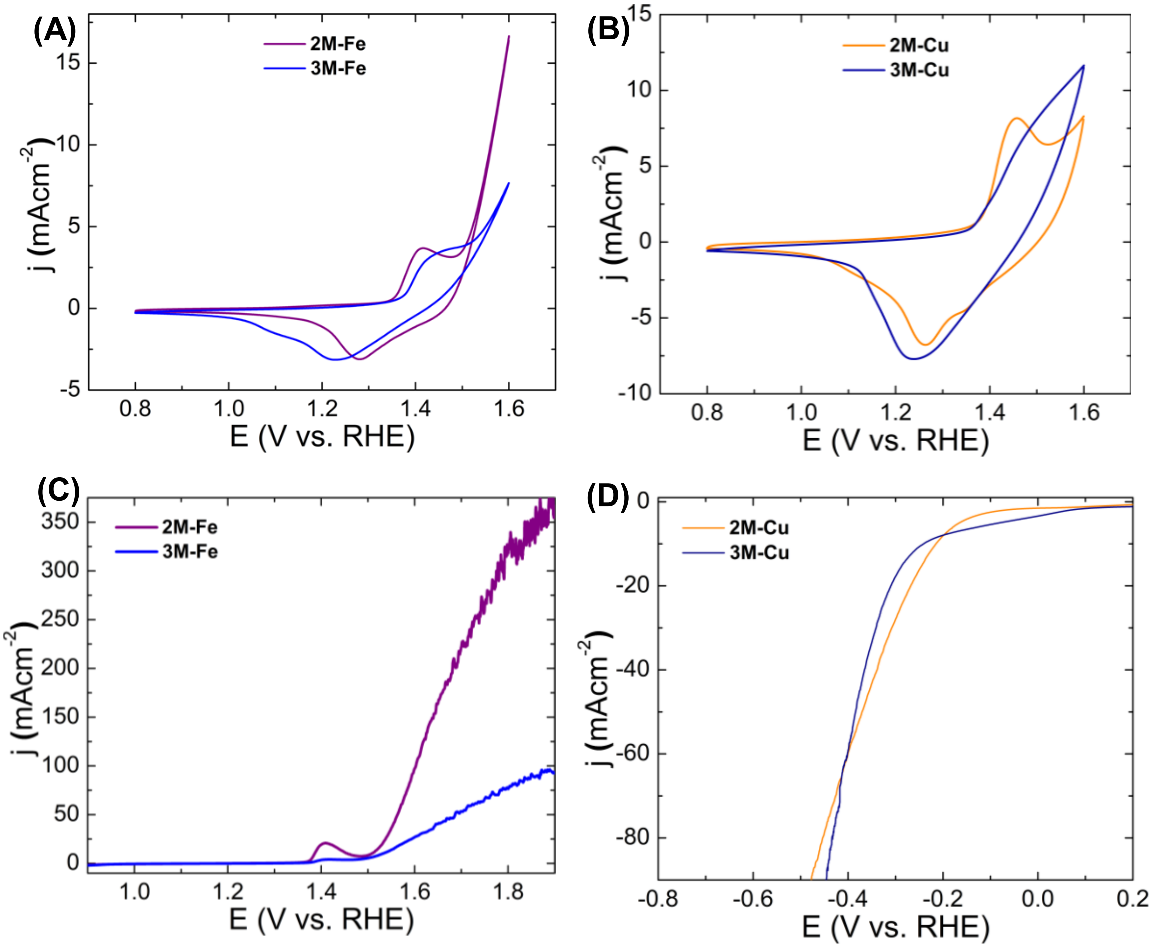

Figure S12. Comparative cyclic voltammogram of the synthesized electrode using 2M and 3M dopant ion solution (A) NiFe electrode (B) NiCu electrodes; Comparative linear sweep polarization curve synthesized electrode using 2M and 3M dopant ion solution (C) NiFe electrode (D) NiCu electrodes.

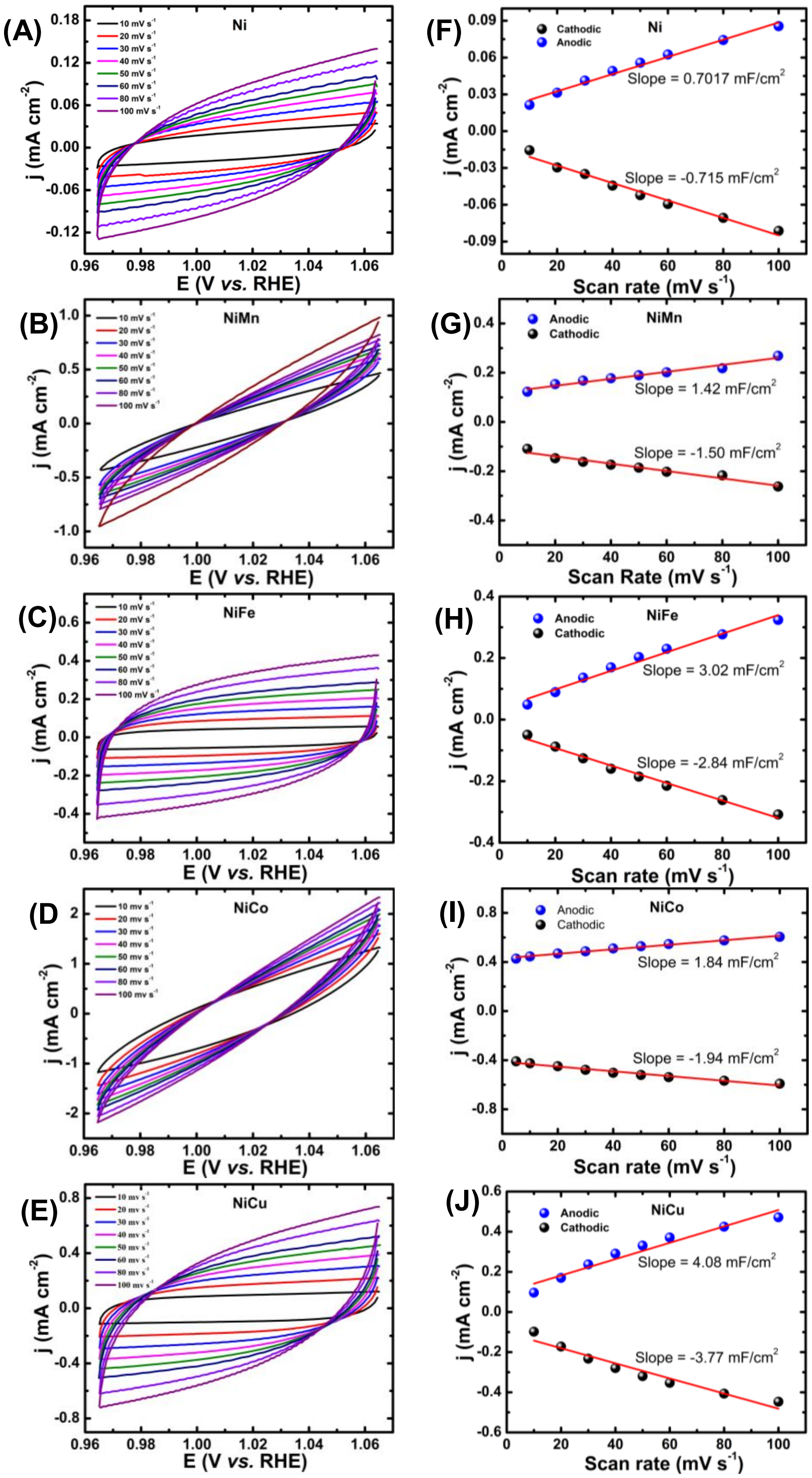

Figure S13. Cyclic voltammetry curves recorded in the non-Faradaic potential region for the catalysts (A) Ni, (B) NiMn, (C) NiFe, (D) NiCo, (E) NiCu, and (F-J) the plot between the anodic and cathodic peak current at 1.015 V versus scan rate to determine the double capacitance (C_{dl}) of the catalysts.

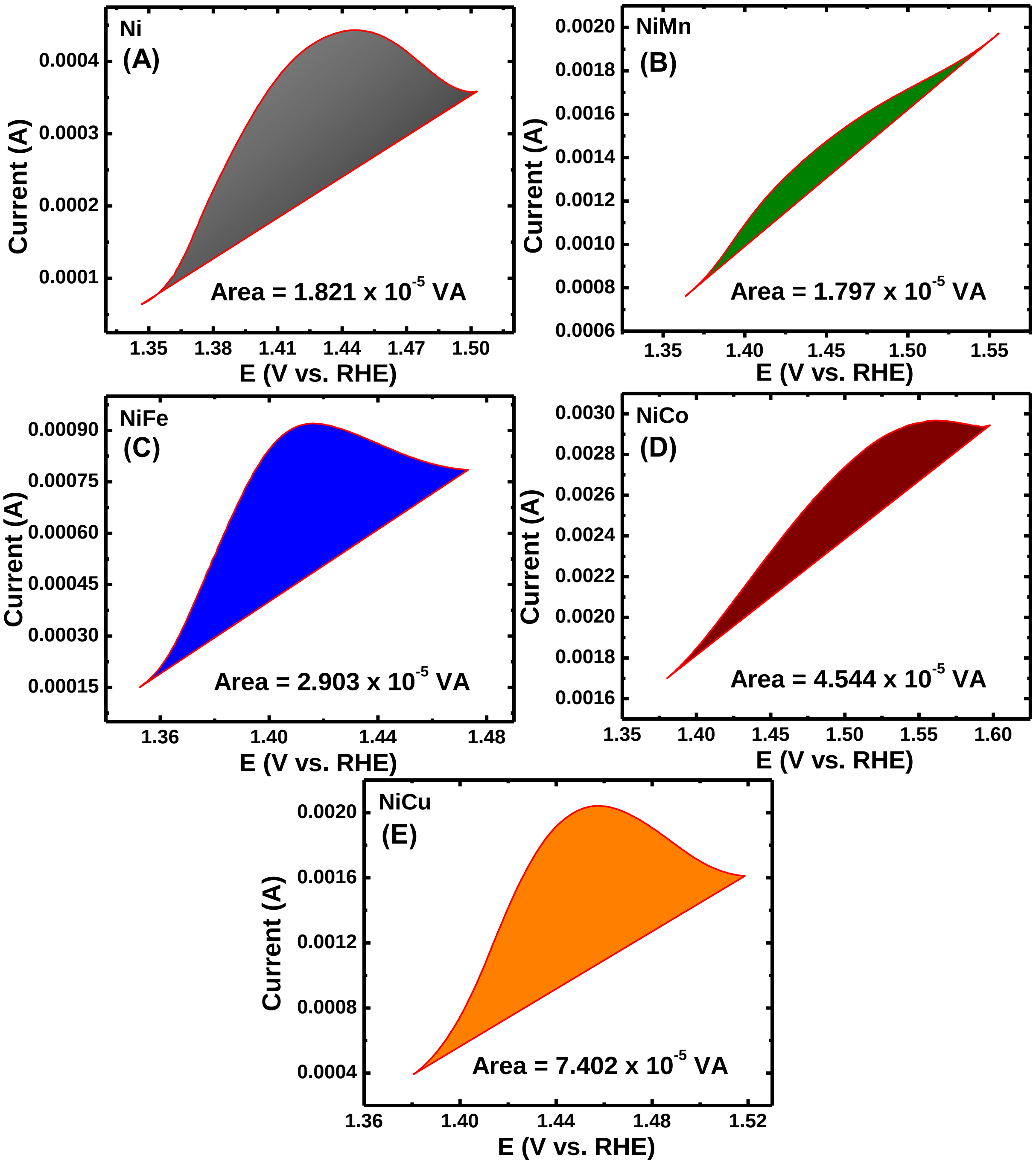

Figure S14. The calculated area associated with the oxidation of Ni^{2+} to Ni^{3+} of (A) Ni, (B) NiMn, (C) NiFe, (D) NiCo, and (E) NiCu catalyst electrodes.

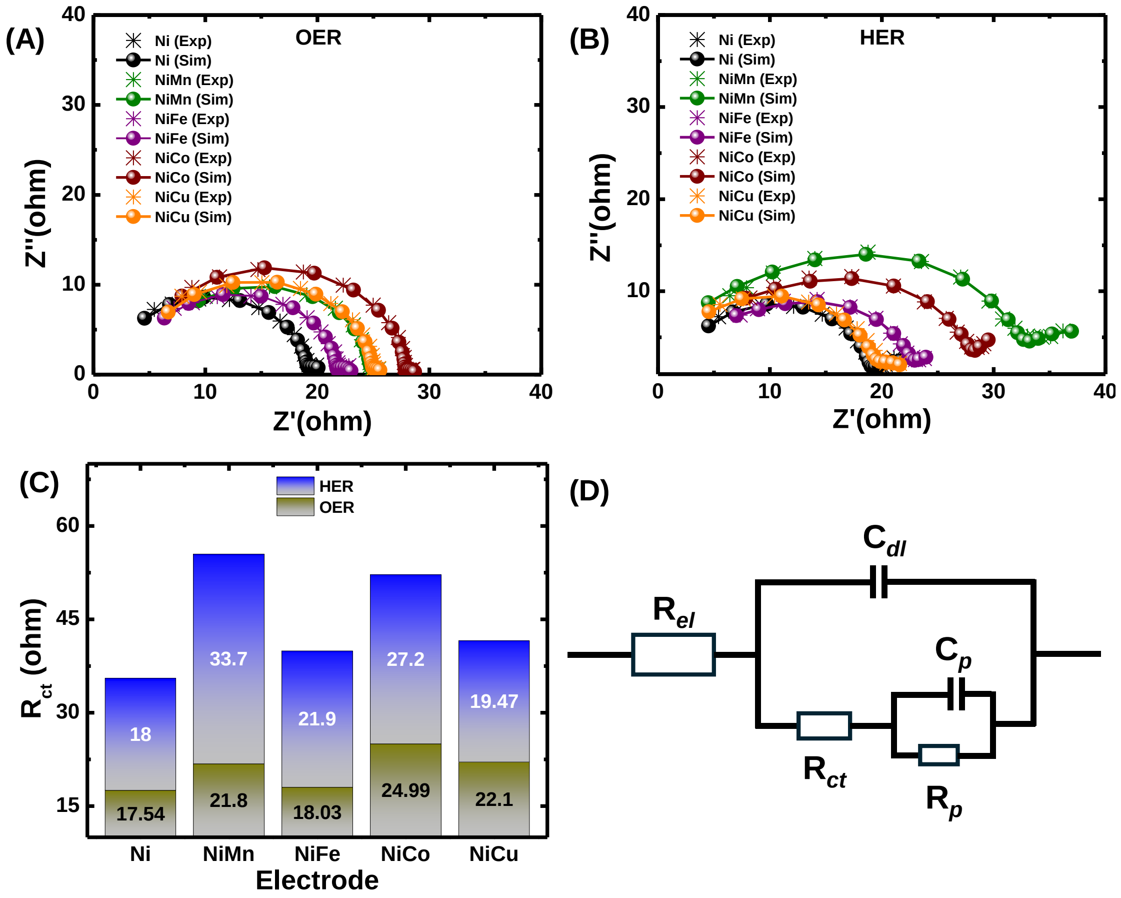

Figure S15. Comparative EIS spectra (A) OER onset, (B) HER onset, (C) R_{ct} comparison, and (D) Fitted circuit for HER/OER charge transfer.

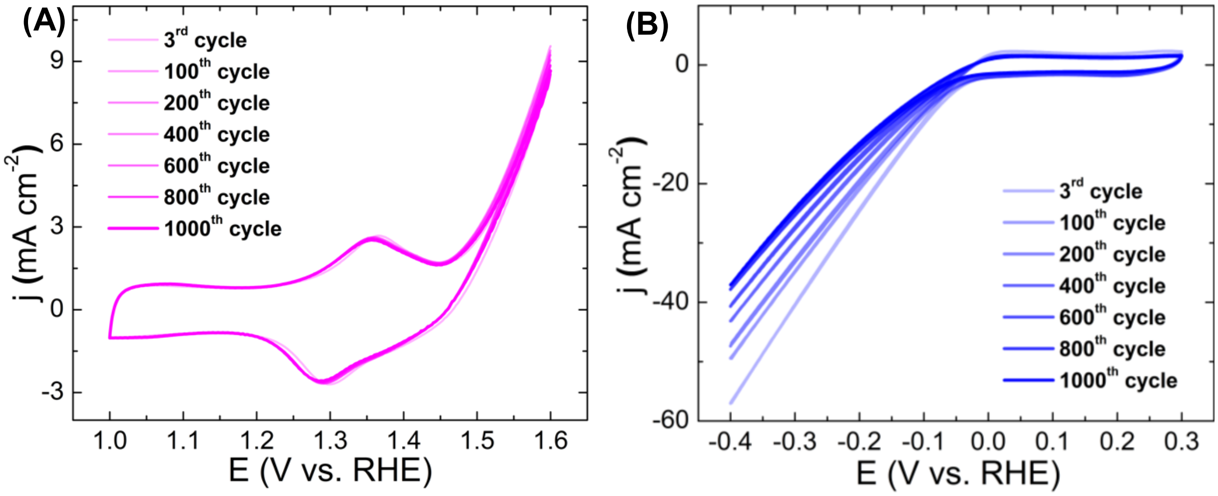

Figure S16. Electrocatalytic durability analysis of the state-of-the-art catalyst electrodes towards OER and HER reactions: (A) accelerated durability CV of the RuO_2 electrode in the OER potential region for 1000 cycles, (B) durability CV cycle of 20% Pt/C electrode for 1000 cycles in the HER potential region.

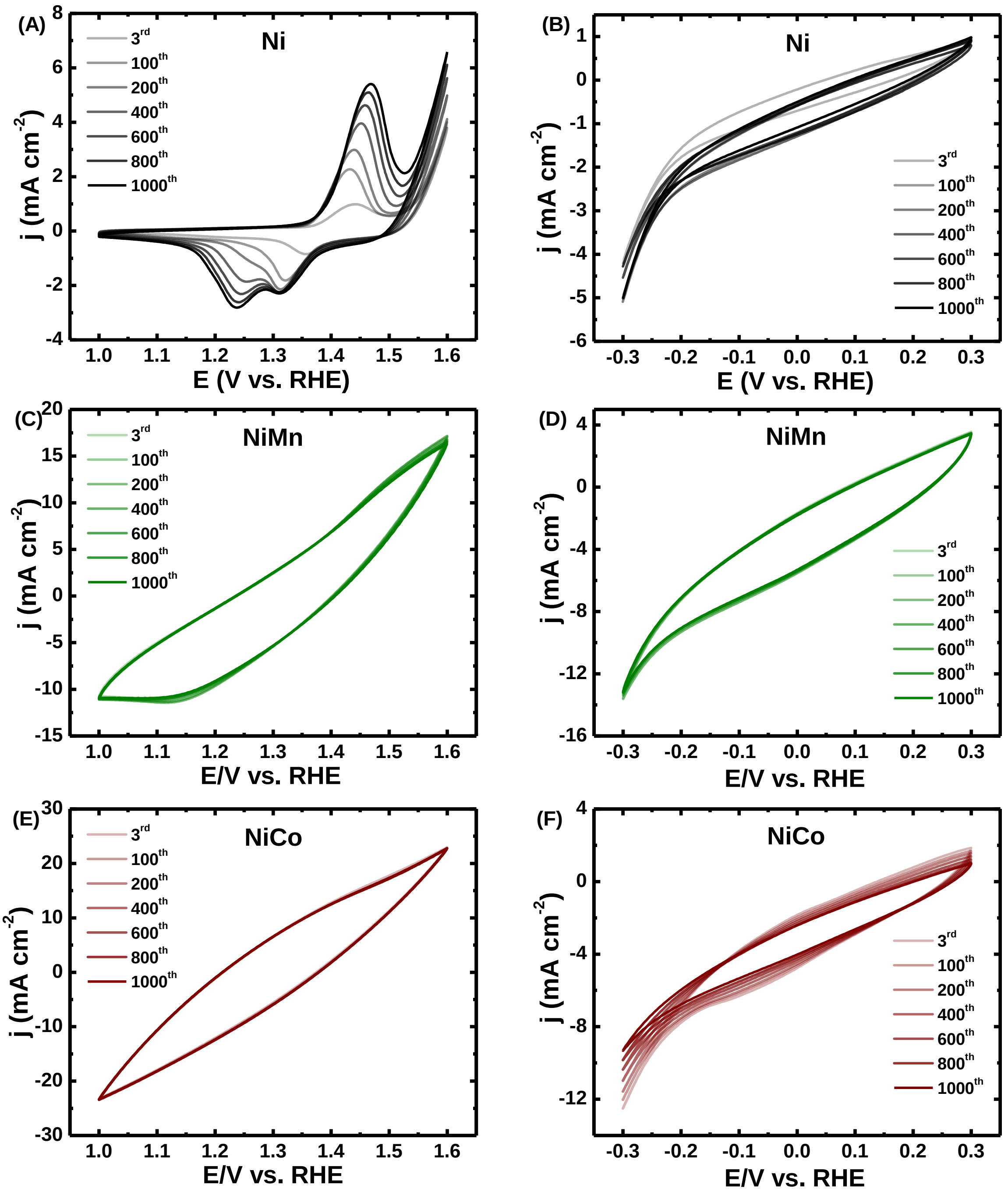

Figure S17. Durability test through 1000 consecutive CV cycles at OER and HER region for electrode: (A, B) Ni, (C, D) NiCu, and (E, F) NiCo at a specific OER and HER respectively.

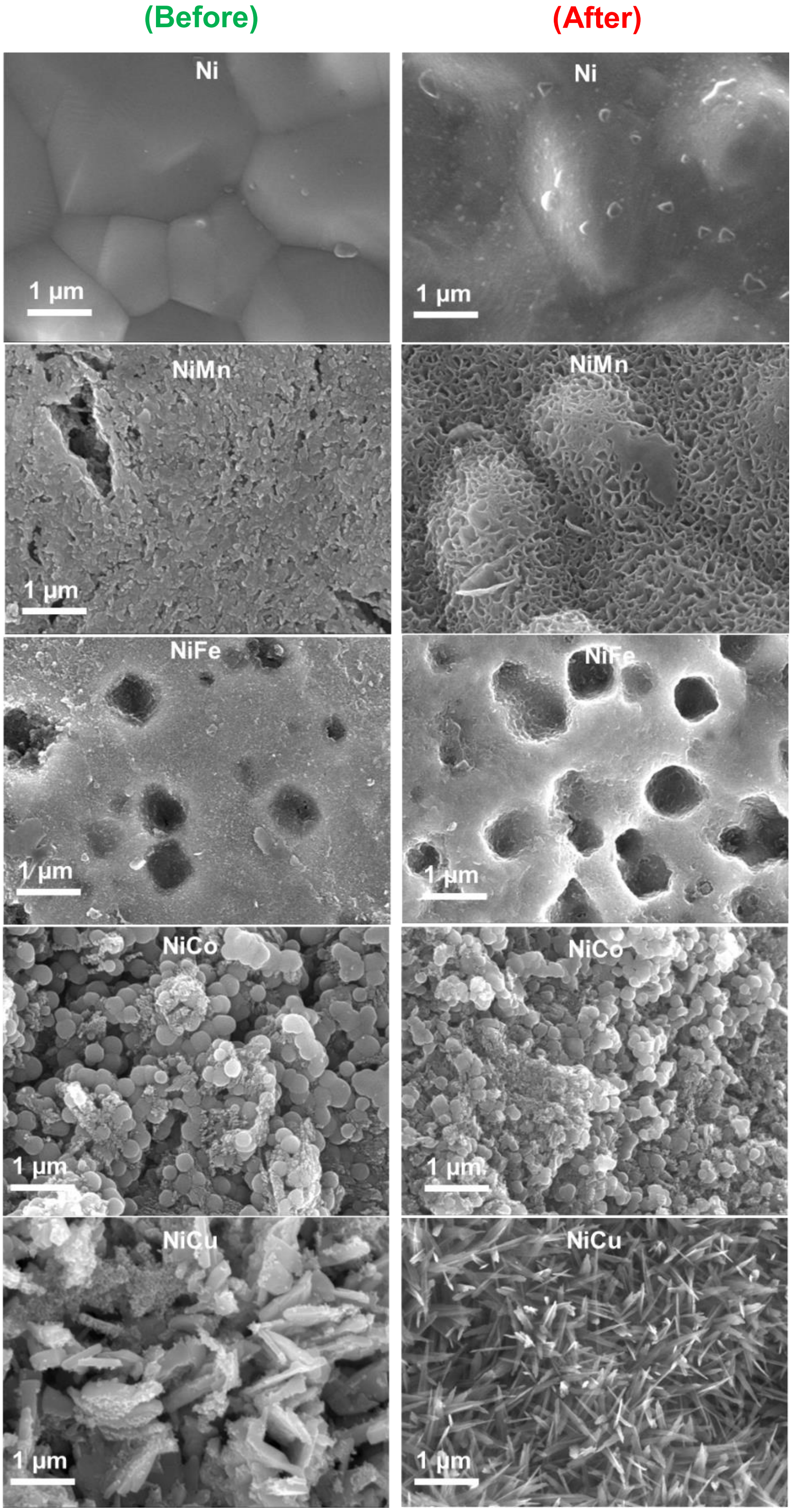

Figure S18. Comparative pre-surface (left panel) and post-surface (right panel) morphology analysis of electrodes after all electrochemical experiments**.**

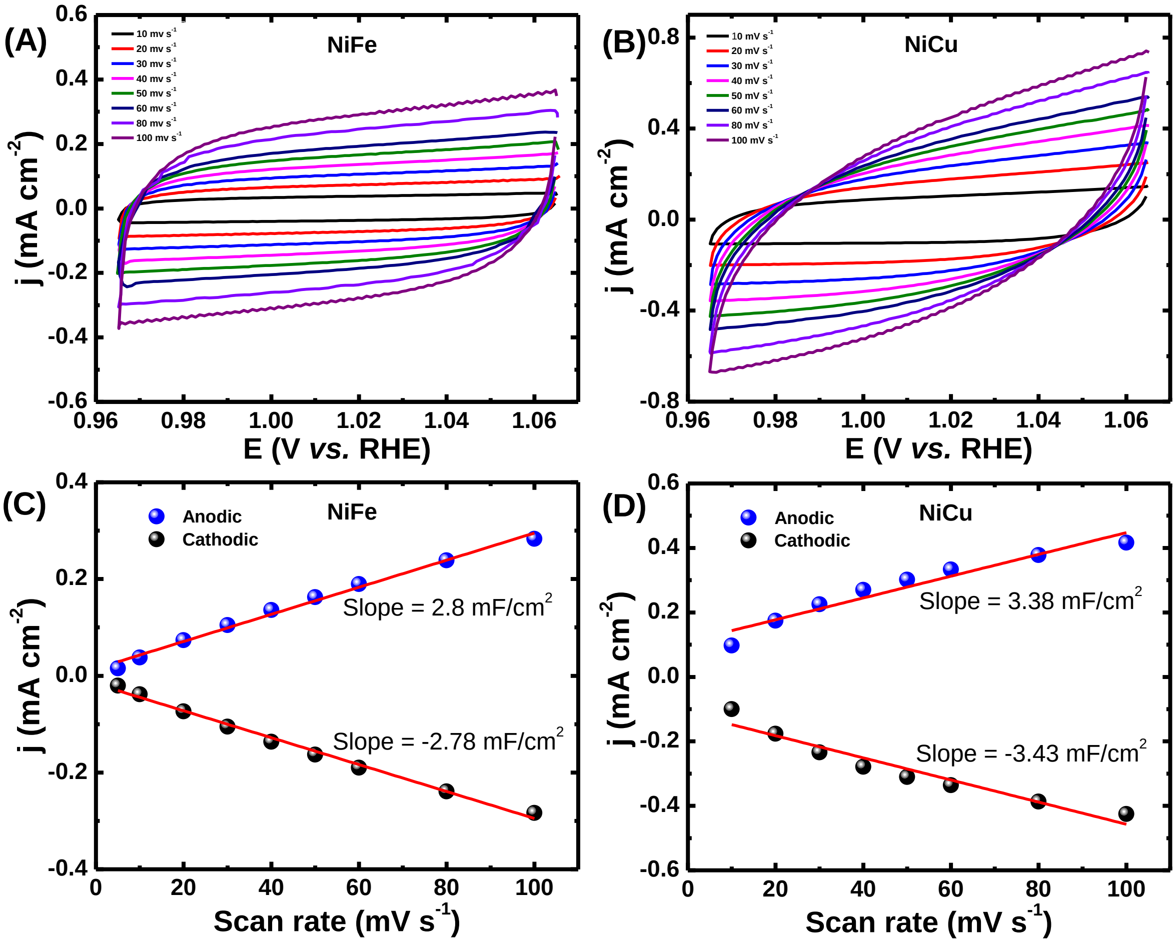

Figure S19. Cyclic voltammetry curves of NiFe and NiCu electrodes after the 5000 cycles CV in OER and HER condition; (A) NiFe, (B) NiCu, and (C, D) are their corresponding plot of Ja and Jc at 1.015 V vs. RHE against scan rate for the determination of double layer capacitance (C_{dl}) of the catalysts, respectively.

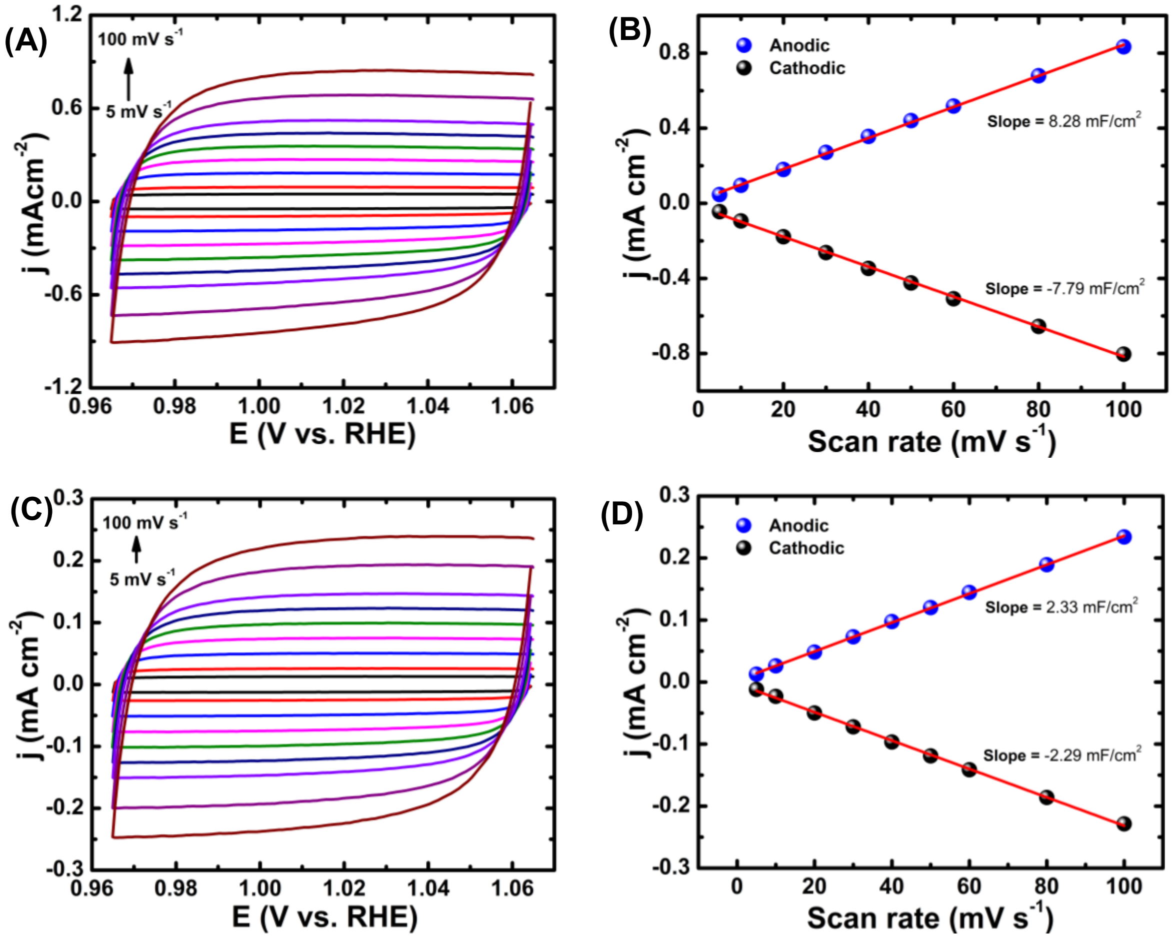

Figure S20. Cyclic voltammetry curves of RuO$_2$ at non-Faradaic potential region; (A) before OER durability; (A) before 1000 cycles CV in OER condition, (B) before durability corresponding plot of Ja and Jc at 1.015 V vs. RHE against scan rate for the determination of double layer capacitance (C$_{dl}$) of the catalysts and (C) after1000 cycles CV in OER condition, and (D) after 1000 cycles CV in OER condition durability corresponding plot of Ja and Jc at 1.015 V vs. RHE against scan rate for the determination of double layer capacitance (C$_{dl}$) of the catalysts.

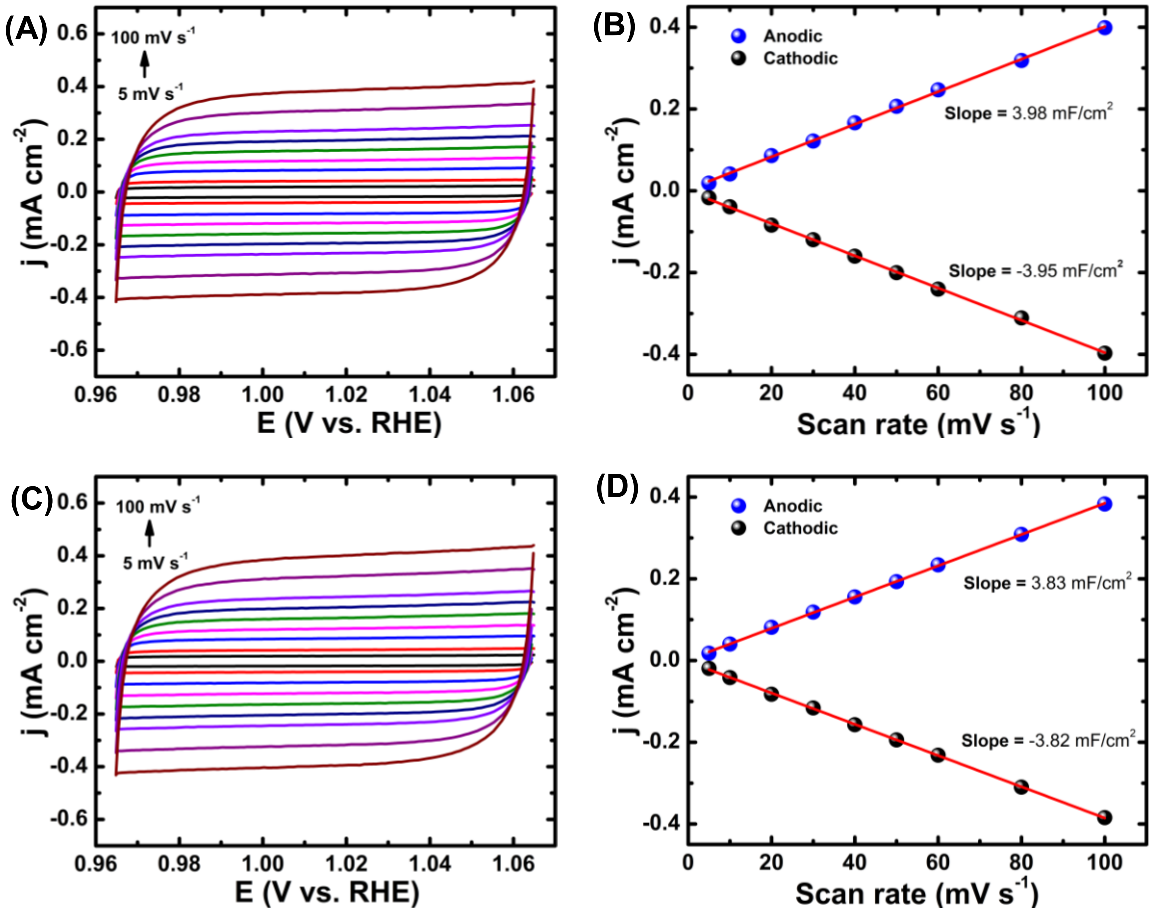

Figure S21. Cyclic voltammetry curves of 20% Pt/C at non-Faradaic potential region; (A) before 1000 cycles CV in HER condition, (B) before durability corresponding plot of Ja and Jc at 1.015 V vs. RHE against scan rate for the determination of double layer capacitance (C_{dl}) of the catalysts and (C) after 1000 cycles CV in HER condition durability CV (D) after durability corresponding plot of Ja and Jc at 1.015 V vs. RHE against scan rate for the determination of double layer capacitance (C_{dl}) of the catalysts.

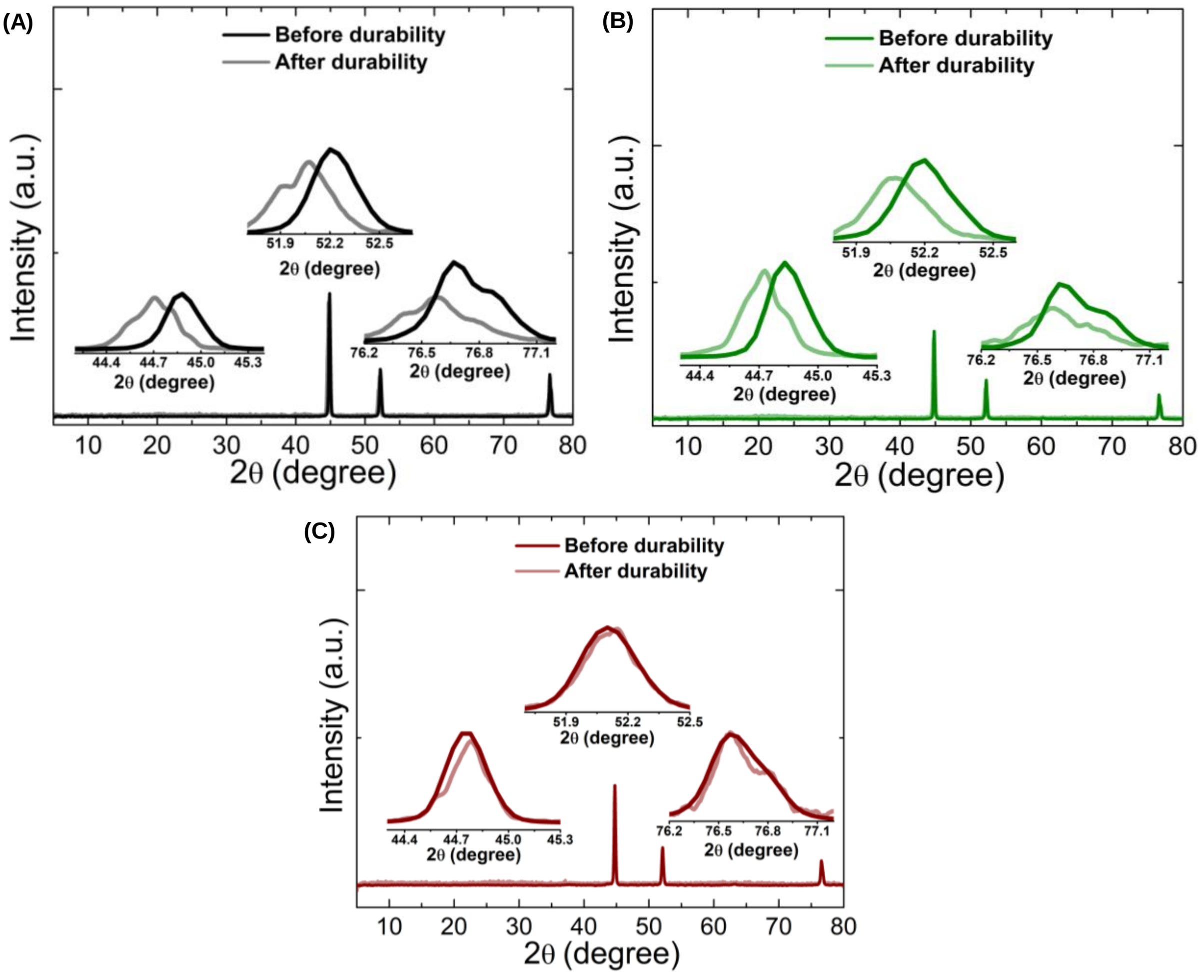

Figure S22. Post-durability PXRD analysis of electrodes after consecutive 1000 cycle CV in OER and HER region durability measurements (a) Ni, (b) NiMn, and (b) NiCo.

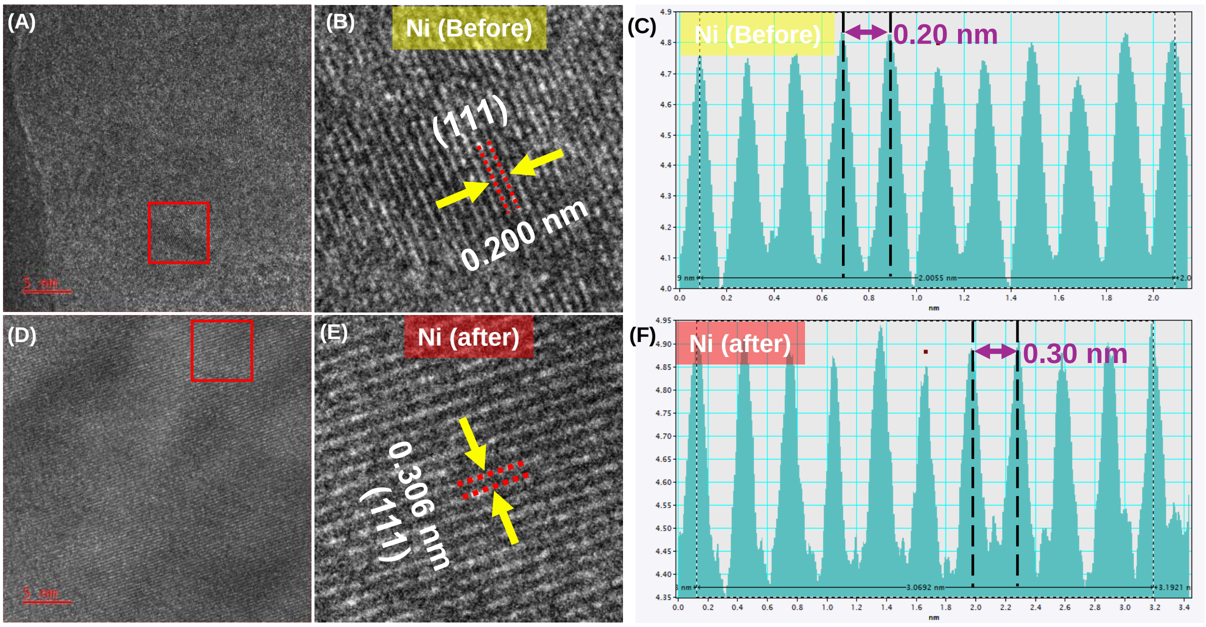

Figure S23. TEM analysis of pristine Ni electrode; (A) TEM image of pristine Ni electrode before electrochemical measurement; (B) HRTEM image of Ni electrode before electrochemical measurement showing the 111 planes of the marked area; (C) Corresponding line pattern of image HRTEM; (D) TEM image of pristine Ni electrode after electrochemical measurement; and (E) HRTEM image of Ni electrode after electrochemical measurement showing the 111 planes of the marked area; (F) corresponding line pattern of image HRTEM.

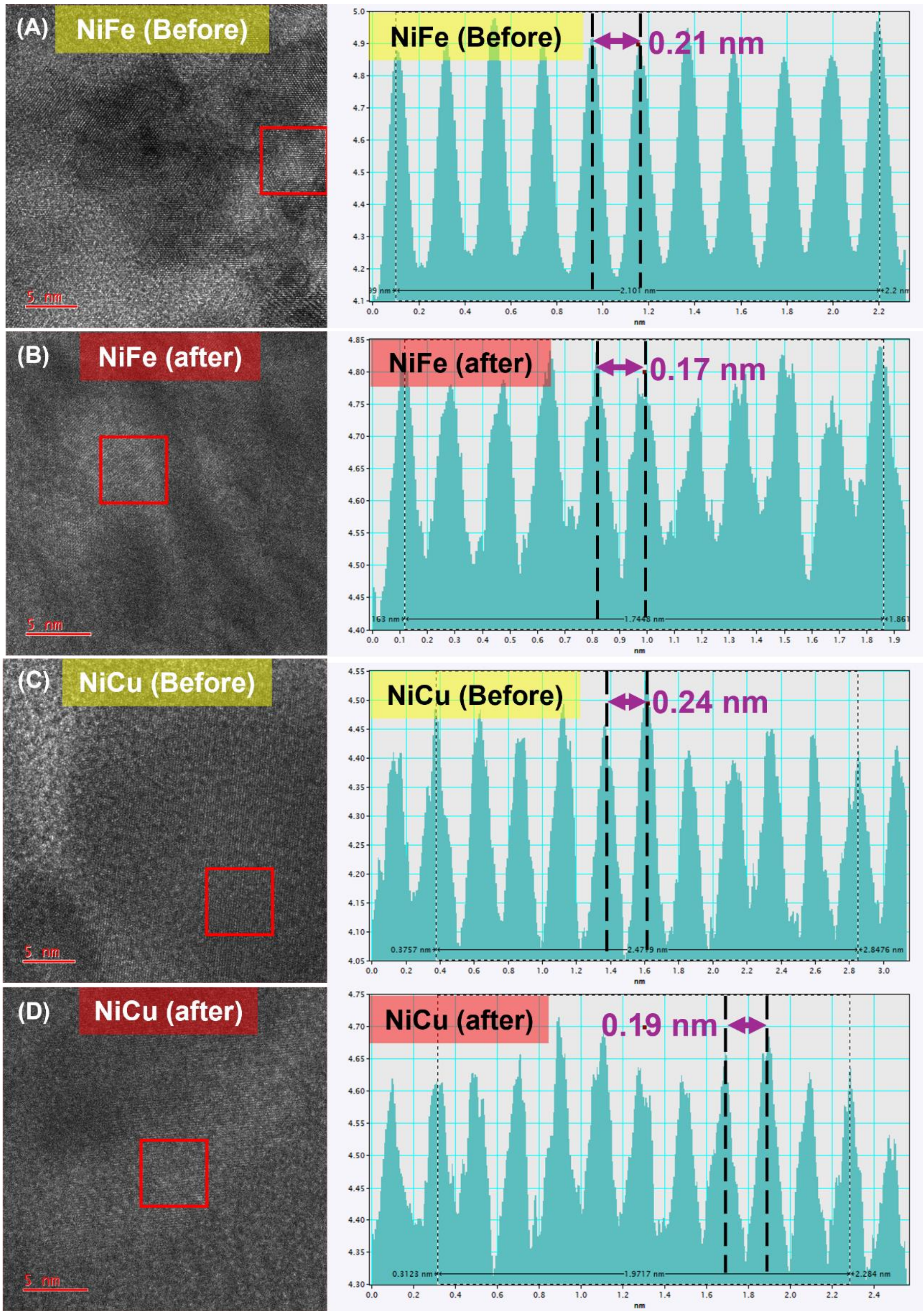

Figure S24. Line pattern of TEM analysis for Ni, NiFe, and NiCu electrode before and after the durability measurement; (A, B) NiFe and (C, D) NiCu electrode.

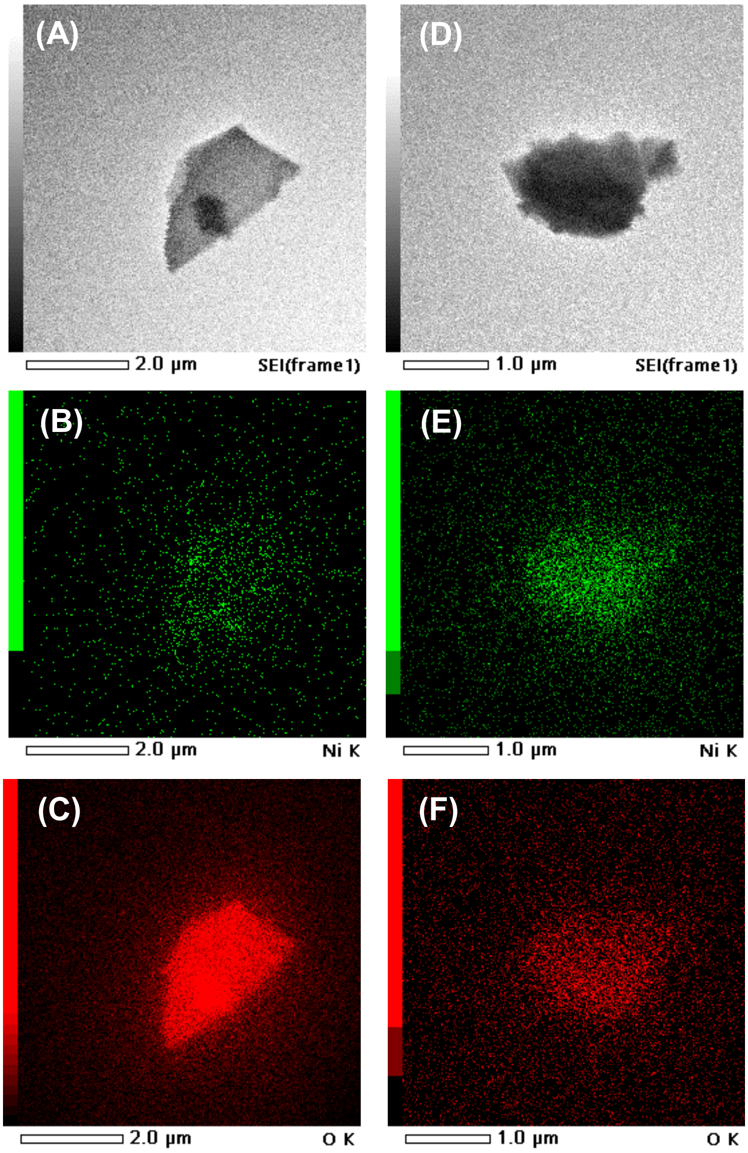

Figure S25. EELS elemental mapping of pristine Ni electrode before electrochemical analysis. (A) SEI image of pristine Ni electrode;(B-C) distribution of Ni, and O. (D) SEI image of pristine Ni electrode after electrochemical measurement, (E, F) distribution of Ni, and O element after electrochemical measurement.

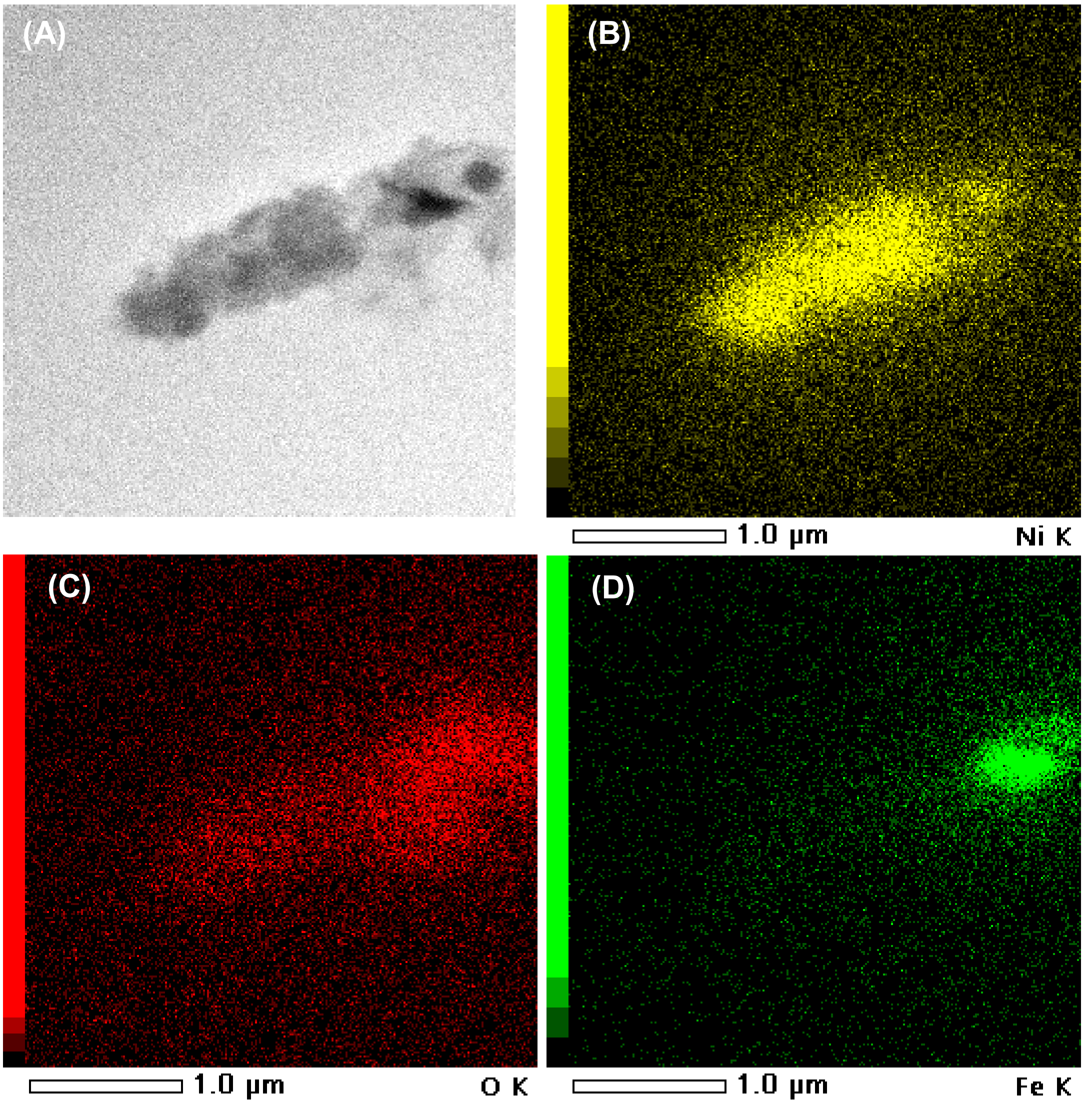

Figure S26. EELS elemental mapping of NiFe electrode after the electrochemical measurement (A) SEI image of NiFe electrode;(B-D) the distribution of Ni, O, and Fe.

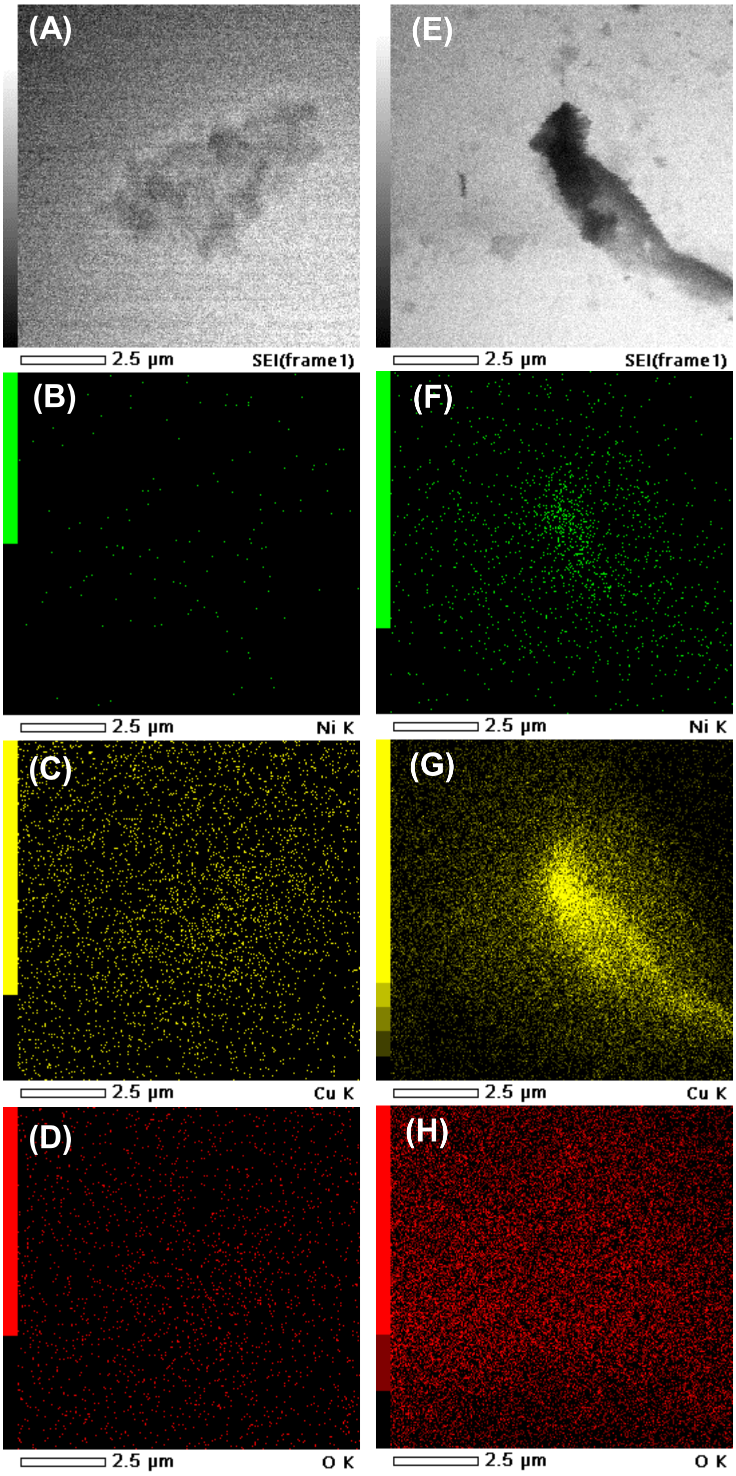

Figure S27. EELS elemental mapping of NiCu electrode (A-D) SEI image of NiCu electrode and elemental distribution of Ni, Cu, and O before all electrochemical measurements; (E-H) SEI image of NiCu electrode and elemental distribution of Ni, Cu, and O after all electrochemical measurements.

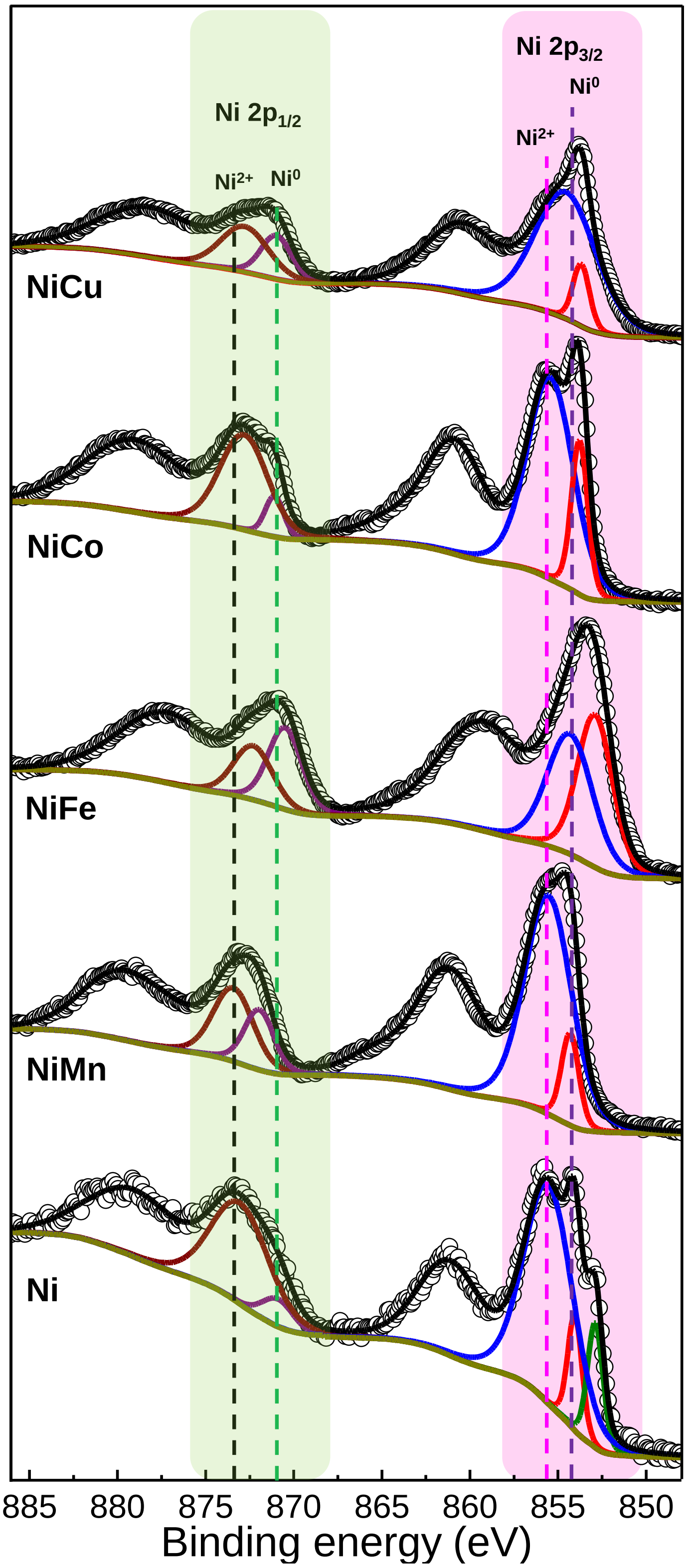

Figure S28. Deconvoluted Ni 2p spectra of Ni, NiMn, NiFe, NiCo, and NiCu electrodes show the shift in binding energy as a result of the de-alloying of heteroatom.

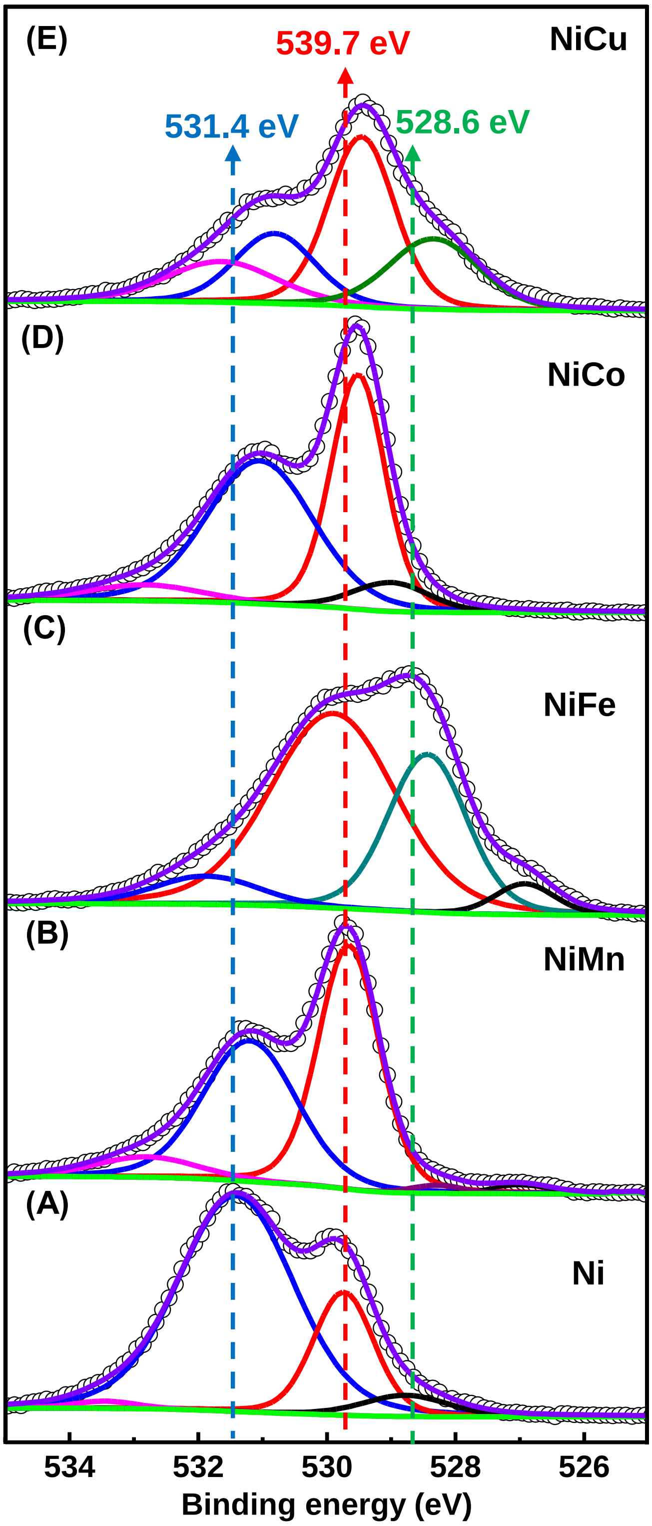

Figure S29. Comparative deconvoluted XPS O 1s spectra after electrochemical durability analysis (A) Ni, (B) NiMn, (C) NiFe, (D) NiCo, and (E) NiCu electrode.

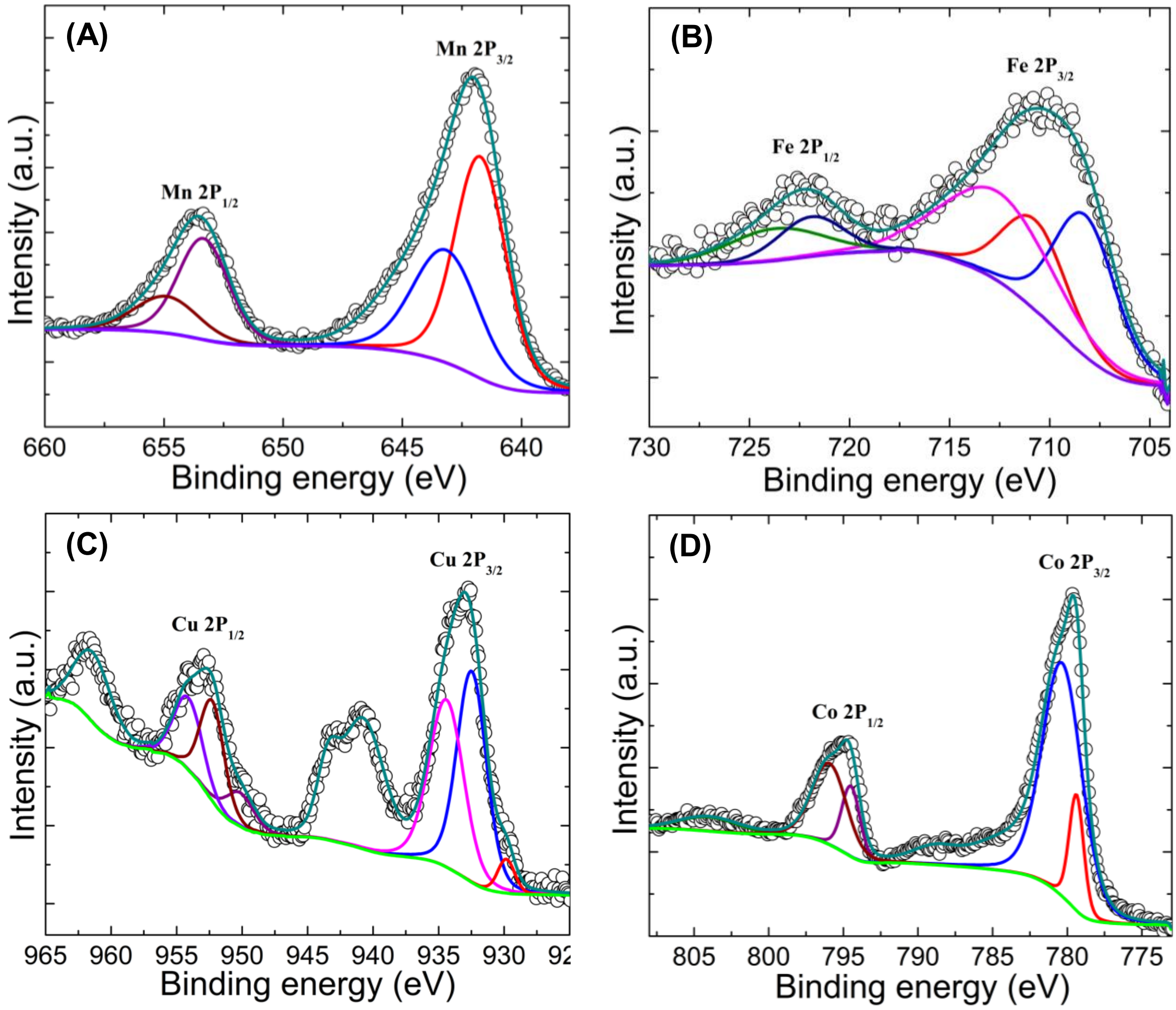

Figure S30. After durability deconvoluted high-resolution X-ray photoelectron spectroscopy (XPS) analysis of the dopant elements present in Ni-M alloy electrode (A) Mn 2p, (B) Fe 2p, (C) Co 2p, and (D) Cu 2p.

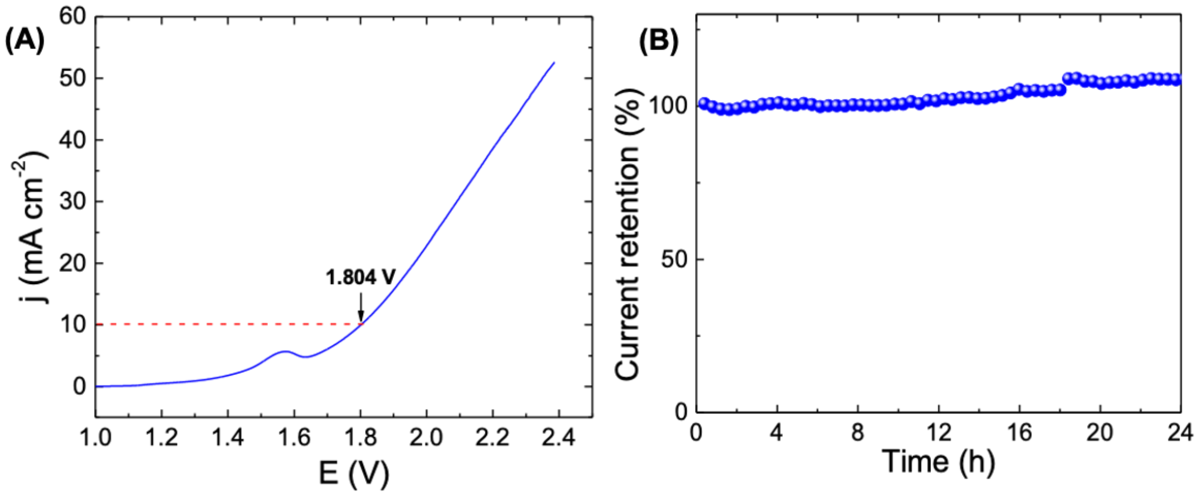

Figure S31: Overall water splitting performance of NiCu||NiFe alloy electrodes; (A) linear sweep voltammogram response, and (B) durability test for overall water splitting performance at 1.8V for 24 h.

Table T1: Overpotential (η) to obtain 10 mA cm^{-2} for the oxygen evolution reaction (OER) of the NiFe active phase catalysts with structure optimization.

Electrocatalyst	**Electrolyte**	η_{OER}^{10} **(mV)**	**Tafel Slop (mV dec^{-1})**	**Ref.**
NiFe-alloy	0.1 M KOH	275	76	This work
HG–NiFe	1 M KOH	310	39	[7]
Bimetallic FeNi	0.1 M KOH	430	56	[8]
NiFe@g-C_3N_4/CNT	1 M KOH	326	67	[9]
$N_{i0.5}Fe_{0.5}$@N-graphite	1 M KOH	210	62	[10]
$Ni_{50}Fe_{50}$@N–CNTs	1 M KOH	318	79	[11]
$FeNi_3$@NC	1 M KOH	277	77	[12]
NiFe@NCNFs	1 M KOH	294	52	[13]
NiFeC-800-5	1 M KOH	269	72	[14]
3D NiFe alloy foams	1 M KOH	240	47	[15]
1D NiFe alloy nanotube array	1 M KOH	236	45	[16]
NiFe@C	1 M KOH	345	57	[17]
NiFe@V_2O_3	1 M KOH	330	51	[18]
Amorphous NiFe	1 M KOH	265	24	[19]
Fcc-phase NiFe alloy	1 M KOH	298	51.9	[20]
Hcp-phase NiFe alloy	1 M KOH	226	41	[21]

Electrocatalyst	**Electrolyte**	η_{OER}^{10} **(mV)**	**Tafel slop (mV dec^{-1})**	**Ref.**
NiCu	0.1 M KOH	216	174	This work
NI-Cu foam	1 M KOH	227	94	[22]
NiCu/rGO	1 M KOH	347	154.6	[23]
NiCu	0.1 M KOH	280	142	[24]
NiCu	1 M KOH	181	146	[25]

Table T2: Overpotential (η) to obtain 10 mA cm^{-2} for the hydrogen evolution reaction (HER) of the NiCu alloy catalysts.

NiCu-alloy	1 M KOH	112	136.2	26
Ni-Cu alloy nanosheets	1 M KOH	128	57.2	27
NiCuOx/NiCuC	1 M KOH	116	155	28
NiCuC	1 M KOH	189	149	28
NiCu-DH	1 M KOH	180	73	29
Ni-Cu-A	1 M KOH	270	93.9	30
Ni-Cu B	1 M KOH	202	82	30

Table T3: Comparison of the electrocatalytic activities of self-supported electrocatalysts for overall water splitting.

Electrocatalyst	η_{OER}^{10} **(mV)**	η_{HER}^{10} **(mV)**	**Cell Voltage (V)**	**Ref.**
Ni_3S_2/VO_2	150	100	1.42	31
Pt/Ni_xFe LDHs	300	100	1.47	32
NiFe LDH@Ni	191	101	1.51	33
Ni@NiFe LDH	218	92	1.53	34
$MoS_2/Co_9S_8/Ni_3S_2$	166	103	1.54	35
Cu@NiFe LDH	199	116	1.54	36

NiFe-UMNs	251	-	1.55	37
Ni_3S_2@MoS_2/FeOOH	234	95	1.57	38
NiFe LDH-NiCoP	220	110	1.57	39
Ni-FeO_x/$FeNi_3$	267 (50 $mAcm^{-2}$)	35	1.58	40
Cobalt iron hydroxide	110	220	1.61	41
N-doped CoP	60	-	1.61	42
δ-FeOOH	265	110	1.62	43
P-doped Co_3O_4	303	97	1.63	44
NiMo	310	92	1.64	45
CoP	30	52	1.65	46
CoS_2	276	193	1.67	47
$NiCo_2S_4$	-	-	1.68	48
Ni_3S_2	-	-	1.73	49
NiFe-NiCu alloy	275	216	1.80	This Work
NiFeOF	295	253	1.80	50
$NiCo_2O_4$			1.84	49

References:

1. N. K. Tyagi, B. K. Mahapatra, S. Ghimire, N. Manna, D. Kumar, V. Kumar, K. Mukhopadhyay, S. K. Singh, *ACS Appl. Energy Mater.* **2023**, *6*, 6111-6119.
2. Poojita, T. Rom, R. Biswas, K. K. Haldar, A. K. J. I. C. Paul, **2024**, *63*, 3795-3806.
3. J. P. Perdew, K. Burke, M. Ernzerhof, *Phys. Rev. Lett.* **1996**, *77*, 3865-3868.
4. G. Kresse, D. Joubert, *Phys. Rev. B* **1999**, *59*, 1758-1775.
5. J. K. Nørskov, T. Bligaard, A. Logadottir, J. R. Kitchin, J. G. Chen, S. Pandelov, U. Stimming, *J. Electrochem. Soc.* **2005**, *152*, J23.
6. R. R. Georg Job, *Physical Chemistry from a Different Angle*, Springer, 1 edn., 2016.

7. J. Wang, L. Gan, W. Zhang, Y. Peng, H. Yu, Q. Yan, X. Xia, X. J. S. a. Wang, *Sci. Adv.* **2018**, *4*, eaap7970.
8. Y. Cheng, S. He, J. P. Veder, R. De Marco, S. z. Yang, Ping Jiang, *ChemElectroChem* **2019**, *6*, 3478-3487.

9. D. Liu, S. Ding, C. Wu, W. Gan, C. Wang, D. Cao, Z. ur Rehman, Y. Sang, S. Chen, X. Zheng, *J. Mater. Chem. A* **2018**, *6*, 6840-6846.
10. P. Liu, D. Gao, W. Xiao, L. Ma, K. Sun, P. Xi, D. Xue, Wang, *J. Mater. Chem. A* **2018**, *28*, 1706928.
11. Y. Chen, J. Peng, W. Duan, G. He, Z. Tang, *ChemElectroChem* **2019**, *11*, 5994-6001.
12. D. Chen, J. Zhu, X. Mu, R. Cheng, W. Li, S. Liu, Z. Pu, C. Lin, S. Mu, *ChemElectroChem* **2020**, *268*, 118729.
13. P. Wei, X. Sun, Q. Liang, X. Li, Z. He, X. Hu, J. Zhang, M. Wang, Q. Li, H. Yang, *ACS Appl. Mater. Interfaces* **2020**, *12*, 31503-31513.
14. J. Ding, Q. Sun, L. Zhong, X. Wang, L. Chai, Q. Li, T.-T. Li, Y. Hu, J. Qian, S. Huang, *Electrochim. Acta* **2020**, *354*, 136716.
15. Q. Kang, D. Lai, W. Tang, Q. Lu, F. Gao, *Chem. Sci.* **2021**, *12*, 3818-3835.
16. C.-L. Huang, X.-F. Chuah, C.-T. Hsieh, S.-Y. Lu, *ACS Appl. Mater. Interfaces* **2019**, *11*, 24096-24106.
17. S.-W. Park, I. Kim, S.-I. Oh, J.-C. Kim, D.-W. J. Kim, *J. Catal*.**2018**, *366*, 266-274.
18. H. Xu, L. Liu, J. Gao, P. Du, G. Fang, H.-J. Qiu, *ACS Appl. Mater. Interfaces* **2019**, *11*, 38746-38753.
19. W. Cai, R. Chen, H. Yang, H. B. Tao, H.-Y. Wang, J. Gao, W. Liu, S. Liu, S.-F. Hung, B. Liu, *Nano lett*. **2020**, *20*, 4278-4285.
20. D. Lim, E. Oh, C. Lim, S. E. Shim, S.-H. Baeck, *J. Catal.* **2020**, *352*, 27-33.
21. C. Wang, H. Yang, Y. Zhang, Q. Wang, *Angewandte Chemie. Int. ed.* **2019**, *58*, 6099-6103.
22. S. Mojabi, S. Sanjabi, *Thin Solid Films* **2022**, *758*, 139415.
23. S. Kamali, M. Zhiani, H. Tavakol, *Renew. Energy* **2020**, *154*, 1122-1131.
24. G. Lan, Z. Liang, M. Deng, M. He, H. Yi, X. Zhu, H. Zhang, X. Chen, X. Ge, *Rus. J. Phys. Chem. A* **2022**, *96*, 3119-3125.
25. A. Kumar, S. K. Purkayastha, A. K. Guha, M. R. Das, S. Deka, *ACS Catal.* **2023**, *13*, 10615-10626.
26. Y. Zhou, Z. Wang, Z. Pan, L. Liu, J. Xi, X. Luo, Y. Shen, *Adv. Mater.* **2019**, *31*, 1806769.
27. M. Gao, C. Yang, Q. Zhang, Y. Yu, Y. Hua, Y. Li, P. Dong, *Electrochim. Acta* **2016**, *215*, 609-616.
28. L. Yu, Y. Dang, J. Zeng, J. He, S. C. Murphy, P. Kerns, S. L. Suib, J. Zhang, Y. Dou, *Appl. Surf. Sci.* **2020**, *515*, 146117.
29. K.-N. Kang, S.-I. Kim, J.-C. Yoon, J. Kim, C. Cahoon, J.-H. J. Jang, *ACS Appl. Mater. Interfaces*, **2022**, *14*, 33013-33023.
30. N. Lotfi, T. Shahrabi, Y. Yaghoubinezhad, G. B. J. Darband, *J. Electroanal Chem.* **2019**, *848*, 113350.
31. Q. Lv, L. Yang, W. Wang, S. Lu, T. Wang, L. Cao, B. Dong, *J. Mater. Chem. A* **2019**, *7*, 1196-1205.
32. X. Yu, J. Guo, B. Li, J. Xu, P. Gao, K. S. Hui, K. N. Hui, H. Shao, *ACS Appl. Mater. Interfaces* **2021**, *13*, 26891-26903.
33. D. Li, G. Hao, W. Guo, G. Liu, J. Li, Q. Zhao, *J. Power Sources* **2020**, *448*, 227434.
34. Z. Cai, X. Bu, P. Wang, W. Su, R. Wei, J. C. Ho, J. Yang, X. Wang, *J. Mater. Chem. A* **2019**, *7*, 21722-21729.
35. Y. Yang, H. Yao, Z. Yu, S. M. Islam, H. He, M. Yuan, Y. Yue, K. Xu, W. Hao, G. Sun, *J. Am. Chem. Soc.* **2019**, *141*, 10417-10430.
36. L. Yu, H. Zhou, J. Sun, F. Qin, F. Yu, J. Bao, Y. Yu, S. Chen, Z. Ren, *Energy Envir. Sci.* **2017**, *10*, 1820-1827.
37. X. Zhao, Y. Yang, Y. Liu, J. Shi, Q. Li, Q. Xu, W. Lin, *Langmuir* **2024**.

38. M. Zheng, K. Guo, W.-J. Jiang, T. Tang, X. Wang, P. Zhou, J. Du, Y. Zhao, C. Xu, J.-S. Hu, *J. Appl. Catal B: Environmnetal* **2019**, *244*, 1004-1012.
39. H. Zhang, X. Li, A. Hähnel, V. Naumann, C. Lin, S. Azimi, S. L. Schweizer, A. W. Maijenburg, R. B. Wehrspohn, *Adv. Funct. Mater.* **2018**, *28*, 1706847.
40. A. Qayum, X. Peng, J. Yuan, Y. Qu, J. Zhou, Z. Huang, H. Xia, Z. Liu, D. Q. Tan, P. K. Chu, *ACS Appl. Mater. Interfaces*, **2022**, *14*, 27842-27853.
41. P. Babar, A. Lokhande, H. H. Shin, B. Pawar, M. G. Gang, S. Pawar, J. H. Kim, *Small* **2018**, *14*, 1702568.
42. Z. Liu, X. Yu, H. Xue, L. Feng, *J. Mater. Chem. A* **2019**, *7*, 13242-13248.
43. B. Liu, Y. Wang, H. Q. Peng, R. Yang, Z. Jiang, X. Zhou, C. S. Lee, H. Zhao, W. Zhang, *Adv. Mater.* **2018**, *30*, 1803144.
44. Z. Wang, H. Liu, R. Ge, X. Ren, J. Ren, D. Yang, L. Zhang, X. Sun, *ACS Catal.* **2018**, *8*, 2236-2241.
45. J. Tian, N. Cheng, Q. Liu, X. Sun, Y. He, A. M. *J. Mater. Chem. A* Asiri, **2015**, *3*, 20056-20059.
46. T. Liu, L. Xie, J. Yang, R. Kong, G. Du, A. M. Asiri, X. Sun, L. Chen, *ChemElectroChem* **2017**, *4*, 1840-1845.
47. C. Guan, X. Liu, A. M. Elshahawy, H. Zhang, H. Wu, S. J. Pennycook, J. Wang, *Nanoscale Horiz.* **2017**, *2*, 342-348.
48. D. Liu, Q. Lu, Y. Luo, X. Sun, A. M. Asiri, *Nanoscale* **2015**, *7*, 15122-15126.
49. A. Sivanantham, P. Ganesan, S. Shanmugam, *Adv. Funct. Mater.* **2016**, *26*, 4661-4672.
50. K. Liang, L. Guo, K. Marcus, S. Zhang, Z. Yang, D. E. Perea, L. Zhou, Y. Du, Y. Yang, *ACS Catal.* **2017**, *7*, 8406-8412.